J. Fluid Mech. (1991), *vol.* 232, *pp.* 469–520
Printed in Great Britain

Analysis of turbulence in the orthonormal wavelet representation

By CHARLES MENEVEAU†
Center for Turbulence Research, Stanford University, Stanford, CA 94305-3030, USA

(Received 9 November 1990 and in revised form 1 May 1991)

A decomposition of turbulent velocity fields into modes that exhibit both localization in wavenumber and physical space is performed. We review some basic properties of such a decomposition, the wavelet transform. The wavelet-transformed Navier–Stokes equations are derived, and we define new quantities such as $e(r,\boldsymbol{x})$, $t(r,\boldsymbol{x})$ and $\pi(r,\boldsymbol{x})$ which are the kinetic energy, the transfer of kinetic energy and the flux of kinetic energy through scale r at position $\boldsymbol{x}$. The discrete version of $e(r,\boldsymbol{x})$ is computed from laboratory one-dimensional velocity signals in a boundary layer and in a turbulent wake behind a circular cylinder. We also compute $e(r,\boldsymbol{x})$, $t(r,\boldsymbol{x})$ and $\pi(r,\boldsymbol{x})$ from three-dimensional velocity fields obtained from direct numerical simulations. Our findings are that the localized kinetic energies become very intermittent in $\boldsymbol{x}$ at small scales and exhibit multifractal scaling. The transfer and flux of kinetic energy are found to fluctuate greatly in physical space for scales between the energy containing scale and the dissipative scale. These fluctuations have mean values that agree with their traditional counterparts in Fourier space, but have standard deviations that are much larger than their mean values. In space (at each scale r), we find exponential tails for the probability density functions of these quantities. We then study the nonlinear advection terms in more detail and define the transfer $T(r\,|\,r',\boldsymbol{x})$ between scale r and all scales smaller than r', at location $\boldsymbol{x}$. Then we define $\pi_{\rm sg}(r,\boldsymbol{x})$, the flux of energy caused only by the scales smaller than r, at $\boldsymbol{x}$, and find negative values for $\pi_{\rm sg}(r,\boldsymbol{x})$ at almost 50% of the physical space at every scale (backscatter). We propose the inclusion of local backscatter in the phenomenological cascade models of intermittency, by allowing some energy to flow from small to large scales in the context of a multiplicative process in the inertial range.

1. Introduction

One of the most instructive ways to look at the physics of turbulence is by transforming the Navier–Stokes equations for incompressible flow

$$\frac{\partial u_i}{\partial t}+u_j\frac{\partial u_i}{\partial x_j}=-\frac{1}{\rho}\frac{\partial p}{\partial x_i}+\nu\frac{\partial^2 u_i}{\partial x_j^2},\quad \frac{\partial u_i}{\partial x_i}=0, \tag{1}$$

to Fourier space:

$$\left(\frac{\partial}{\partial t}+\nu k^2\right)\hat{u}_i(\boldsymbol{k})=-ik_k P_{ij}(\boldsymbol{k})\int_{\boldsymbol{q}} u_j(\boldsymbol{q})\,u_k(\boldsymbol{k}-\boldsymbol{q})\,d^3\boldsymbol{q}, \tag{2}$$

$$P_{ij}(\boldsymbol{k})=\delta_{ij}-\frac{k_i k_j}{k^2}.$$

---

† Present address: Department of Mechanical Engineering, Johns Hopkins University, Baltimore, MD 21218, USA.

Here u_i and p are the fluctuating parts of the velocity and pressure, and we have omitted terms containing the mean velocity, body forces, etc. The velocity field $\boldsymbol{u}$ is represented as a linear combination of plane waves, each corresponding to a characteristic size $(\sim k_i^{-1})$ in some direction i. However, information related to position in physical space is completely hidden, which is a disadvantage when dealing with spatial intermittency in the flow. On the other hand, without performing operations involving multiple points, the Navier–Stokes equations in physical space give no explicit information about different scales of motion, information that is often a useful ingredient for modelling and physical insight. This difficulty calls for a representation that decomposes the flow field into contributions of different scales as well as different locations. In other words, we want to use basis functions that behave more like localized pulses than extended waves. Additional requirements such as self-similarity lead to rather special basis functions, called wavelets, which are generated by translations and dilations of a single function.

The wavelet transform has generated much interest, and most of the relevant theory has been developed only quite recently. Continuous wavelet analysis was introduced by Grossmann & Morlet (1984), and has been applied to several fields (e.g. to sound analysis by Kronland-Martinet, Morlet & Grossmann 1987). A recent review of wavelets appears in Farge (1992). In the field of turbulence, the potential of wavelet analysis has been pointed out in the context of coherent structures by Farge & Rabreau (1988) and it has been used to study turbulent multifractal nature in Bacry *et al.* (1990). A detailed wavelet analysis of two-dimensional data from a turbulent jet can be found in Everson, Sirovich & Sreenivasan (1990). These studies use the continuous wavelet transform. Starting with the work of Meyer (1986) several orthonormal wavelet basis functions have been constructed (Daubechies 1988) which are convenient in practical applications (Mallat 1989) especially in higher dimensions, because no redundant information is generated.

The traditional discrete Fourier transform maps a three-dimensional function sampled on e.g. N^3 points onto $\frac{1}{2}N^3$ complex Fourier coefficients (conserving the amount of information N^3). From this, useful and compact statistical information can be extracted as power-spectra of the field, either the radial spectrum, or separate spectra in the different Cartesian directions. The usefulness of this approach stems from a variety of reasons including: (*a*) the existence of the fast Fourier transform, which allows efficient calculation of the transform (this also has permitted the manufacture of appropriate hardware such as digital spectral analysers); (*b*) the straightforward interpretation of the power-spectral density as related to the squared amplitude of waves in which the field is being decomposed; (*c*) the fact that the discrete Fourier transform is used not only as a tool of analysis, but also to solve partial differential equations (e.g. with the pseudospectral method (Orszag & Patterson 1972) for the Navier–Stokes equations). Other basis functions such as Chebychev polynomials are often employed to deal with particular boundary conditions; for the purpose of the present discussion, however, we consider them to be of the same family as the Fourier modes owing to their global nature.

Orthonormal wavelet functions have the property that they also conserve information, that is, a discretely sampled field on N^3 points will yield only N^3 coefficients. However, these will be organized in a fashion that allows distinction between scale and location. This property is best illustrated in one dimension: here we have a total of N gridpoints, and thus N coefficients: $\frac{1}{2}N$ of them give information at $\frac{1}{2}N$ different locations about the smallest scale, $\frac{1}{4}N$ on the spatial distribution at the next larger scale, etc. The last coefficient is related to the global mean of the field.

This dyadic arrangement not only makes sense physically (the larger scales are sampled more coarsely than the smaller ones), but it also allows for the implementation of a fast algorithm, analogous to the fast Fourier transform.

The objective of the present work is to propose an analysis of turbulence using the orthonormal wavelet decomposition rather than the Fourier transform. In order for the analysis to be practical, we have to achieve significant reductions in the amount of data. In the case of the three-dimensional Fourier transform, where we start with N^3 values, the spectra essentially reduce to a single-valued function consisting of $O(N)$ points. This is easy to visualize and to interpret physically. Here we obtain more than the spectrum, using the additional spatial information that is now available. In this work the focus will be purely statistical, but the idea is to postpone spatial averaging as long as possible. In comparison with the discrete Fourier analysis the orthonormal wavelet approach has the following properties: (*a*) there is an efficient fast wavelet algorithm allowing the computation of all the coefficients with at most $O(N \log N)$ operations (for some wavelets, the operation count can be as low as $O(N)$!); (*b*) the interpretation of the square of the coefficients as the energy of localized pulses is straightforward and very intuitive; (*c*) statistical properties (or more detailed spatial characterizations) of these coefficients, in addition to the power-spectrum, can be obtained and are easy to visualize and interpret. So far then, there is no practical difference between Fourier and wavelet analysis, but the latter allows more meaningful analysis of spatial properties at every scale, which is of great importance in the case of turbulence. The other important point raised in connection with the usefulness of the discrete Fourier transform, namely that it can play a key role in actually solving the equations, cannot be made so far with the wavelet basis functions (there are several preliminary efforts in that direction, e.g. to use wavelets to solve Burgers equation (see e.g. Farge 1992), but it is a little early to be sure of their practicality in this context). Therefore, for the time being, we concentrate only on properties (*a*), (*b*) and (*c*) listed above, which are worth exploring in the hope of characterizing turbulent flow fields in a systematic fashion.

The idea of studying turbulence using a space and scale dependence is not new: it was the motivation for band-pass filtering turbulent signals, an approach that was employed to study intermittency (see e.g. Kennedy & Corrsin 1961). Such studies were decisive in showing that turbulent activity becomes more and more intermittent at smaller and smaller scales, as quantified by appropriate statistical measures, such as flatness factors. However, such methods of analysis are rather arbitrary in terms of the shape of filters, their bandwidth, etc. Here we attempt to circumvent this arbitrariness by invoking the more rigorous foundations of orthonormal wavelet analysis, which has the prospect of becoming a more standardized tool.

The relative simplicity of the analysis of turbulence with wavelets stems from the fact that they are generated from a single function, known *a priori*, and this therefore does not depend on the specific flow. This is in contrast to the method of 'proper orthogonal decomposition' (Lumley 1967), which constructs basis functions that maximize the energy contained in the smallest number of modes. Here we do not attempt any such optimization, and so the number of wavelets needed is generally high. However, such an approach is necessary to study local properties of instantaneous realizations of turbulent flows, because for example in the case of homogeneous flows, the proper orthogonal decomposition yields the usual non-local Fourier modes.

We also point out that several previous studies (Siggia 1977; Zimin 1981; Nakano 1988) attempt the use of 'wave packets' for obtaining meaningful approximations to the Navier–Stokes equations, and then deduce energy cascade models. These studies use self-similar wave packets, so that they are essentially equivalent to wavelets. We believe that it is necessary to complement such efforts with measurements in actual turbulent flows, using similar basis functions. This may provide better guidance for modelling the nonlinear interactions. Also, we notice that spatially compact octave filters (again in essence equal to wavelets) were used by Sulem & Frisch (1975) to establish a rigorous bound (equal to $-\frac{8}{3}$) for the inertial-range exponent of the turbulent energy spectrum, required to guarantee that the spectral flux does not vanish at high Reynolds numbers.

After having outlined the conceptual reasons for proposing orthonormal wavelets as a tool for statistical analysis of turbulence, we turn now to the more physical questions to be addressed in this paper. One of the most important features of a turbulent flow is the transfer of kinetic energy from large to small scales of motion. For isotropic turbulence, the three-dimensional energy spectrum $E(k,t)$ (Monin & Yaglom 1971) obeys

$$\frac{\partial E(k,t)}{\partial t} = T(k,t) - 2\nu k^2 E(k,t), \tag{3}$$

where $T(k,t)$ is the net transfer of energy to wavenumbers of magnitude k. $T(k,t)$ is formally defined in terms of triple products of fluctuating velocity and thus embodies the closure problem resulting from the nonlinearity of the equations. The total spectral flux of energy through wavenumber k to all smaller scales is given by

$$\pi(k,t) = \int_k^\infty T(k',t)\,\mathrm{d}k' = -\int_0^k T(k',t)\,\mathrm{d}k'. \tag{4}$$

The usual arguments of equilibrium and stationarity lead to the condition that in the 'inertial range' $\eta \ll k^{-1} \ll L$, where L is the integral scale and η is the Kolmogorov microscale, the ensemble average of the flux must equal the overall rate of dissipation:

$$\langle \pi(k,t) \rangle_{\mathrm{ens}} = \epsilon. \tag{5}$$

Usually the mechanism of energy transfer is visualized by simplified models such as the successive break-down of 'eddies', or as the creation of small scales by the stretching and folding of vortical elements. One then argues that through scales of motion of size k^{-1}, there is a net flux of kinetic energy to smaller scales, which is equal to the time average of $\pi(k,t)$. Notice that $\pi(k,t)$ does not depend on position because of the Fourier representation used to obtain (5). If one now wishes to reconcile this definition of a 'flux' of energy to smaller scales with the phenomenological picture of breakdown of eddies, one needs to tacitly make the assumption that its average value $\langle \pi(k,t) \rangle$ is indeed physically representative of the underlying physics in every region of space. In some loose sense, this corresponds to the theory of Kolmogorov (1941), which neglects the phenomenon of intermittency.

It has been known for a long time (Batchelor & Townsend 1949) that the rate of dissipation $\epsilon(x,t)$ is distributed very intermittently (a behaviour which increases with the Reynolds number of the flow), and that its moments increase with Reynolds number according to power-laws in the inertial range (see e.g. Kolmogorov 1962; Novikov 1971; Mandelbrot 1974). This permits a self-consistent statistical and geometrical representation of ϵ in terms of multifractals (Parisi & Frisch 1985; Benzi *et al.* 1984; Meneveau & Sreenivasan 1987*a*, *b*; Meneveau & Sreenivasan 1991, hereinafter referred to as I). The observation of power-law behaviour of spatial moments of the dissipation can be modelled rather naturally within the framework of break-down of eddies, but now assuming that the flux of energy to smaller scales exhibits spatial fluctuations. These fluctuations accumulate as the scales of motion become smaller, and can lead to very intermittent distributions of the dissipation. This suggests the need for defining a flux of kinetic energy which, as opposed to (4), should retain some information about spatial locality. This cannot be achieved with Fourier modes, and provides us with a specific motivation for the use of wavelets to define new quantities related to the energy dynamics of turbulence. Using the wavelet representation of the velocity field, we will introduce quantities that are analogous to the Fourier spectra of energy $E(k,t)$, transfer $T(k,t)$ and energy flux $\pi(k,t)$, but which depend on location as well as scale. These quantities can be used in several ways, e.g. to correlate specific local events with possible structures or topological features of the flow field. In this paper we will restrict our attention to statistical descriptions of the spatial distribution of these quantities. These are easy to compute and to interpret, and do not depend on specific views about what the underlying structures of turbulence are.

The calculations are performed on three-dimensional fields from direct numerical simulations of isotropic flow and homogeneous shear flow and measurements in two laboratory wind-tunnel experimental velocity signals (boundary layer and wake behind a circular cylinder).

Section 2 provides a brief review of wavelets intended for the reader not familiar with this formalism. We cover the continuous transform, wavelet series and the discrete wavelet transform in one dimension and extend the basic ideas to three dimensions. The focus is on the orthonormal representation that will be used in the subsequent analysis of turbulent flow fields. In §3, we write the Navier–Stokes equations in the wavelet representation both in terms of continuous and discrete transforms. Appropriate contractions of the equations lead to an evolution equation for the local kinetic energy involving a nonlinear local transfer at every scale. The distribution of kinetic energy and transfer are studied in the next sections.

In §4, we perform the wavelet analysis of the turbulent kinetic energy using experimental and numerical data sets. From the laboratory measurements, we also attempt to quantify the intermittency of the kinetic energy using notions of multifractal distributions. Section 5 deals with the transfer and flux of kinetic energy in the wavelet representation, where the appropriate data is taken from the three-dimensional flow fields obtained from numerical simulations. In §6 we address some issues related to the transfer and flux to (or from) the small scales only, an analysis that is relevant for subgrid-scale modelling. Section 7 then re-examines the usual phenomenological models of intermittency to incorporate the new features encountered in §§5 and 6. Finally, a summary and the conclusions are presented in §8. Useful details about the implementation of fast wavelet algorithms in one and three dimensions, the different types of wavelets used and appropriate windowing algorithms are described in the Appendices of Meneveau (1990). Also, a brief account of some of the findings reported here has already been given in Meneveau (1991).

2. The wavelet transform

2.1. *Continuous wavelet transform*

Given a signal $f(x)$, its wavelet transform is defined as

$$w(r,x) \equiv W_{(r,x)}[f] = C_{\psi}^{-\frac{1}{2}} r^{-\frac{1}{2}} \int_{-\infty}^{\infty} \psi^{*}\left(\frac{x'-x}{r}\right) f(x')\,\mathrm{d}x', \tag{6}$$

where $\psi(x)$ is a function called a wavelet, satisfying the admissibility condition

$$C_{\psi} = \int_{-\infty}^{\infty} |k|^{-1} |\hat{\psi}(k)|^{2}\,\mathrm{d}k < \infty. \tag{7}$$

Here $\hat{\psi}(k)$ is the Fourier transform of $\psi(x)$,

$$\hat{\psi}(k) = \int_{-\infty}^{\infty} \psi(x)\,\mathrm{e}^{-\mathrm{i}kx}\,\mathrm{d}x. \tag{8}$$

The wavelet $\psi(x)$ has zero mean, will have some oscillations, and can be real or complex. A typical example of a real wavelet is the mexican hat $\psi(x) = (1-x^{2})\exp(-\frac{1}{2}x^{2})$, which can be viewed as the difference between two exponentials of different sizes centred around $x = 0$. The wavelet transform $w(r,x)$ can thus be interpreted as the relative contribution of scales r to the signal at position x, and is similar to the Gabor transform (or 'short-time' Fourier transform), which uses a translating function of fixed width (giving the spatial localization) and another modulating function (such as $\mathrm{e}^{2\pi\mathrm{i}kx}$) for which the wavenumber is varied. The main difference is that the wavelet involves only one generating function $\psi(x)$ providing translations and dilations simultaneously to reduce the spatial support at the same rate at which the frequency is increased (or scale decreased).

If the wavelet is admissible ($\psi(x)$ obeys condition (7)), the wavelet transform can be inverted as (Grossmann & Morlet 1984)

$$f(x) = C_{\psi}^{-\frac{1}{2}} \int_{0}^{\infty} \int_{-\infty}^{\infty} r^{-\frac{1}{2}} \psi\left(\frac{x-x'}{r}\right) w(r,x')\,\frac{\mathrm{d}x'\,\mathrm{d}r}{r^{2}}. \tag{9}$$

In principle (6) could also be inverted from suitable subsets of the (r,x')-plane, for instance at some fixed r_0. One then obtains a Fredholm integral equation of the first kind, with its associated problems especially if the wavelet has narrow support in Fourier space, and so, in practice, it is convenient to consider the entire (r,x')-plane. Another property of the continuous wavelet transform is a generalization of Parseval's theorem (Grossmann & Morlet 1984)

$$\int_{-\infty}^{\infty} f_1(x) f_2^{*}(x)\,\mathrm{d}x = C_{\psi}^{-1} \int_{0}^{\infty} \int_{-\infty}^{\infty} w_1(r,x)\, w_2(r,x)^{*}\,\frac{\mathrm{d}x\,\mathrm{d}r}{r^{2}}, \tag{10}$$

of which the equality of energy in physical and wavelet space is a special case (here * stands for complex conjugate).

As a (band-pass) filter which decays to zero rather quickly, the wavelet transform commutes with differentiation in the spatial variable, namely

$$\frac{\partial}{\partial x} W_{(r,x)}[f] = W_{(r,x)}[f']. \tag{11}$$

For vector functions $\boldsymbol{f}(x)$ with components $f_i(x)$, the transform is a vector $\boldsymbol{w}(r,x)$ whose components are the transforms of the components of $\boldsymbol{f}(x)$.

The wavelet transform $w(r,x)$ can also be obtained from $\hat{f}(k)$, the Fourier transform of $f(x)$ as

$$w(r,x) = C_\psi^{-\frac{1}{2}}(2\pi)^{-1}r^{\frac{1}{2}}\int_{-\infty}^{\infty} \hat{\psi}(rk)^*\hat{f}(k)\,\mathrm{e}^{\mathrm{i}xk}\,\mathrm{d}k. \tag{12}$$

One can also compute $\hat{f}(k)$ from $w(r,x)$ (alternative inversion formula) using the Fourier transform of (9)

$$\hat{f}(k) = C_\psi^{-\frac{1}{2}}\int_0^\infty\int_{-\infty}^{\infty} r^{\frac{1}{2}}\hat{\psi}(rk)\,\mathrm{e}^{-\mathrm{i}xk}w(r,x')\frac{\mathrm{d}x'\,\mathrm{d}r}{r^2}. \tag{13}$$

2.2. *Higher dimensions*

For functions defined in higher dimensions, there are several possibilities. One can consider, in addition to the dilations and translations, the (group of) rotations of non-isotropic wavelets. For the sake of simplicity we consider here spherically symmetric wavelets only, and therefore eliminate the angular dependence. An example of such a higher-dimensional isotropic wavelet is the mexican hat,

$$\psi(\boldsymbol{x}) = (1-|\boldsymbol{x}|^2)\exp\tfrac{1}{2}(-|\boldsymbol{x}|^2). \tag{14}$$

In what follows we write the transforms, inverse transforms and relations to the Fourier descriptions. These expressions will be needed in the next chapter for the formal derivation of the wavelet transformed Navier–Stokes equations.

The three-dimensional transform is:

$$w(r,\boldsymbol{x}) \equiv W_{(r,\boldsymbol{x})}[f] = C_\psi^{-\frac{1}{2}}r^{-\frac{3}{2}}\int_{-\infty}^{\infty}\psi\left(\frac{\boldsymbol{x}'-\boldsymbol{x}}{r}\right)f(\boldsymbol{x}')\,\mathrm{d}^3\boldsymbol{x}', \tag{15}$$

where $\psi(\boldsymbol{x}) = \psi(|\boldsymbol{x}|)$ for the isotropic wavelet. The inversion formula is

$$f(\boldsymbol{x}) = C_\psi^{-\frac{1}{2}}\int_0^\infty\int_{-\infty}^{\infty}\int_{-\infty}^{\infty}\int_{-\infty}^{\infty} r^{-\frac{3}{2}}\psi\left(\frac{\boldsymbol{x}-\boldsymbol{x}'}{r}\right)w(r,\boldsymbol{x}')\frac{\mathrm{d}^3\boldsymbol{x}'\,\mathrm{d}r}{r^4}. \tag{16}$$

Invariance of energy is now written as:

$$\int_{-\infty}^{\infty}\int_{-\infty}^{\infty}\int_{-\infty}^{\infty} f(\boldsymbol{x})^2\,\mathrm{d}^3\boldsymbol{x} = C_\psi^{-1}\int_0^\infty\int_{-\infty}^{\infty}\int_{-\infty}^{\infty}\int_{-\infty}^{\infty} w(r,\boldsymbol{x})^2\frac{\mathrm{d}^3\boldsymbol{x}\,\mathrm{d}r}{r^4}. \tag{17}$$

The wavelet transform $w(r,\boldsymbol{x})$ can also be obtained from $\hat{f}(\boldsymbol{k})$, the Fourier transform of $f(\boldsymbol{x})$, as

$$w(r,\boldsymbol{x}) = C_\psi^{-\frac{1}{2}}(2\pi)^{-3}r^{\frac{3}{2}}\int_{-\infty}^{\infty}\int_{-\infty}^{\infty}\int_{-\infty}^{\infty}\hat{\psi}(r\boldsymbol{k})^*\hat{f}(\boldsymbol{k})\exp(\mathrm{i}\boldsymbol{x}\cdot\boldsymbol{k})\,\mathrm{d}^3\boldsymbol{k}, \tag{18}$$

and this can be inverted as

$$\hat{f}(\boldsymbol{k}) = C_\psi^{-\frac{1}{2}}\int_0^\infty\int_{-\infty}^{\infty}\int_{-\infty}^{\infty}\int_{-\infty}^{\infty} r^{\frac{3}{2}}\hat{\psi}(r\boldsymbol{k})\exp(-\mathrm{i}\boldsymbol{x}\cdot\boldsymbol{k})\,w(r,\boldsymbol{x})\frac{\mathrm{d}^3\boldsymbol{x}\,\mathrm{d}r}{r^4}. \tag{19}$$

Again, because of the translational property of the wavelet transform, differentiation commutes:

$$\boldsymbol{\nabla}\cdot\boldsymbol{W}_{(r,\boldsymbol{x})}[\boldsymbol{f}] = W_{(r,\boldsymbol{x})}[\boldsymbol{\nabla}\cdot\boldsymbol{f}], \tag{20}$$

and
$$\nabla W_{(r,x)}[f] = W_{(r,x)}[\nabla f]. \tag{21}$$

The continuous wavelet transform has proved to be useful in many aplications, see Kronland-Martinet *et al.* (1987) and Farge & Rabreau (1988) to mention just a few. Notice that in the case of one-dimensional signals, the field is represented or unfolded into a two-parameter space (scale and position) and much redundant information is generated. This need not be a problem *per se*, and there are many instances when this is an advantage. In the context of turbulence, however, the number of degrees of freedom in three dimensions is extremely high to start with, thus we need a decomposition that does not increase the size of the database.

2.3. *Wavelet series*

Instead of a continuous transform, a function can be decomposed into a discrete set of orthonormal basis functions. Again, one is interested in a set of self-similar functions, whose dilations and translations provide simultaneous resolution in scale and position. By using a logarithmically uniform spacing of scales with increasingly coarser spatial discretization at larger scales, such bases can be made orthogonal and complete. These requirements have led (see Meyer 1986; Daubechies 1988; Mallat 1989) to the definition of basis functions of the form

$$\psi^{(m)}_{[i]}(x) = a_0^{-\frac{1}{2}m}\psi\left(\frac{x-ib_0\,a_0^m}{a_0^m}\right), \tag{22}$$

where m is a variable scale index and i is a variable position index (not to be confused with $\surd -1$). The parameter a_0 is the base of the dilations and b_0 is the translation length in units of a_0^m. Notice that now the net translation depends on the dilation. The choice for a_0 and b_0 is not completely arbitrary (Daubechies 1988); here we will use the simplest case $a_0 = 2$ and $b_0 = 1$ and thus consider all scales along octaves 2^m and all translations $2^m i$ in multiples of the scale $r_m = 2^m$. In terms of the uncertainty principle for wave packets, this means that the wavelets obey the following constraint at every m:

$$\Delta x_m \,\Delta\left(\frac{1}{r_m}\right) = 2^m(2^{-(m-1)}-2^{-m}) = 1. \tag{23}$$

At smaller scales (larger wavenumber), the spatial resolution becomes better, but we lose resolution in terms of the wavenumber. Also, we will deal only with real wavelets (it has been argued that the phase of a complex wavelet contains important information, but it appears to us that while a phase angle is useful for specifying spatial shifts for waves – i.e. specifying the right mix of sines and cosines – this goal is accomplished in the case of a real wavelet by its translations anyway).

2.3.1. *One-dimensional case*

For one-dimensional signals, one decomposes the function into a discrete set of contributions of different scales and locations according to

$$f(x) = \sum_{m=-\infty}^{\infty}\sum_{i=-\infty}^{\infty} w^{(m)}[i]\,\psi^{(m)}(x-2^m i), \tag{24}$$

where
$$\psi^{(m)}(x) = 2^{-\frac{1}{2}m}\psi\left(\frac{x}{2^m}\right). \tag{25}$$

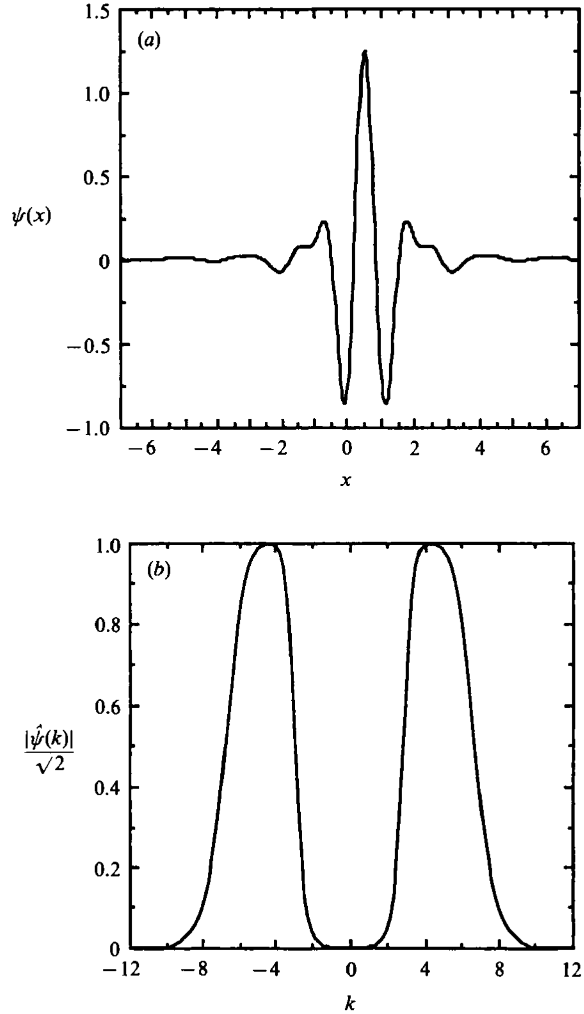

FIGURE 1. (*a*) Example of an orthonormal wavelet basis function $\psi(x)$ (LMB wavelet of order $n = 4$) having exponential decay in physical space. (*b*) The modulus of its Fourier transform $\hat{\psi}(k)$.

The function $\psi(x)$ to be employed has the remarkable property that it is orthonormal to its own translates and its own dilations. In other words,

$$\int_{-\infty}^{\infty} \psi^{(m)}(x-2^m i)\,\psi^{(n)}(x-2^n j)\,\mathrm{d}x = \delta_{ij}\,\delta_{mn}. \tag{26}$$

Evidently, only very special functions will have this property. The simplest one is the Haar basis, $\psi(x) = 1$ for $0 < x \leqslant \frac{1}{2}$, $\psi(x) = -1$ for $\frac{1}{2} < x < 1$ and $\psi(x) = 0$ elsewhere. However, one would like smoother basis functions, preferably with better locality in Fourier space (the Haar basis is compact in physical space, but not in Fourier space where it decays very slowly as k^{-1}).

Functions which meet these requirements have been discovered only recently (Meyer 1986; Daubechies 1988). A brief description of the conditions that they must satisfy and pointers on how they can be constructed can be found in Daubechies (1988) and Appendix B of Meneveau (1990, hereinafter referred to as II). Figure 1 shows one of them, the wavelet constructed by Lemarie & Meyer and by Battle (see

Mallat 1989); for short notation, we will call it from now on the LMB wavelet. Also shown is the modulus of its Fourier transform. The wavelet has exponential decay in physical space and a k^{-4} decay in Fourier space. Since it is well localized both in physical space and in scale coordinates, it provides a reasonably sharp decomposition of the signal into contributions of scale and position. The localization is limited to bands both in x and k space (these bands cannot both have zero thickness because of the uncertainty principle).

Because of (26), we can compute the discrete wavelet coefficients for the function $f(x)$ as

$$w^{(m)}[i] = \int_{-\infty}^{\infty} \psi^{(m)}(x-2^m i) f(x)\, \mathrm{d}x. \tag{27}$$

Therefore, the coefficient $w^{(m)}[i]$ measures the contribution to the signal of scales 2^m in the neighbourhood of the point $2^m i$. Orthonormality implies that total energy obeys

$$\int_{-\infty}^{\infty} f(x)^2\, \mathrm{d}x = \sum_{m=-\infty}^{\infty} \sum_{i=-\infty}^{\infty} (w^{(m)}[i])^2. \tag{28}$$

2.3.2. *Three-dimensional case*

To obtain practical representations in higher dimensions, it is useful to consider separable basis functions, that is, we use basis functions of the form

$$\Psi(\boldsymbol{x}) = \psi_1(x_1)\, \psi_2(x_2)\, \psi_3(x_3), \tag{29}$$

where $x_i\ (i = 1, 2, 3)$ are the three Cartesian coordinates. We still retain the idea of using scales of the form 2^m but must now consider all locations in three-dimensional space. It turns out that for a complete representation one also must consider additional internal degrees of freedom. These complement the function formed by the product of the wavelets along the three Cartesian directions as in (29) The details are given in Appendix A of II, and here we simply note that it is necessary to use 7 distinct basis functions (indexed by q). This additional requirement can be understood intuitively by noting that in one dimension an increase in scale by a factor two decreases the number of gridpoints by a factor of two, the difference of information being provided by the wavelets of the next scale. In three dimensions the reduction is a factor of eight, the difference in information thus requires 7 distinct wavelet coefficients. Now the position is indexed by the triplet indices $[i_1, i_2, i_3]$ (denoted compactly as $[\boldsymbol{i}]$), and the scale is indexed by m, as before. One defines

$$\Psi^{(m,q)}[\boldsymbol{x}-2^m\boldsymbol{i}] = \begin{cases} \psi^{(m)}(x_1-2^m i_1)\, \psi^{(m)}(x_2-2^m i_2)\, \psi^{(m)}(x_3-2^m i_3) & q = 1; \\ \psi^{(m)}(x_1-2^m i_1)\, \psi^{(m)}(x_2-2^m i_2)\, \phi^{(m)}(x_3-2^m i_3) & q = 2; \\ \psi^{(m)}(x_1-2^m i_1)\, \phi^{(m)}(x_2-2^m i_2)\, \psi^{(m)}(x_3-2^m i_3) & q = 3; \\ \psi^{(m)}(x_1-2^m i_1)\, \phi^{(m)}(x_2-2^m i_2)\, \phi^{(m)}(x_3-2^m i_3) & q = 4; \\ \phi^{(m)}(x_1-2^m i_1)\, \psi^{(m)}(x_2-2^m i_2)\, \psi^{(m)}(x_3-2^m i_3) & q = 5; \\ \phi^{(m)}(x_1-2^m i_1)\, \psi^{(m)}(x_2-2^m i_2)\, \phi^{(m)}(x_3-2^m i_3) & q = 6; \\ \phi^{(m)}(x_1-2^m i_1)\, \phi^{(m)}(x_2-2^m i_2)\, \psi^{(m)}(x_3-2^m i_3) & q = 7. \end{cases} \tag{30}$$

The function $\phi^{(m)}(x-2^m i)$ is called a 'smoothing function', which is also generated by translations and dilations of a single function according to

$$\phi^{(m)}(x) = 2^{-\frac{1}{2}m} \phi\left(\frac{x}{2^m}\right). \tag{31}$$

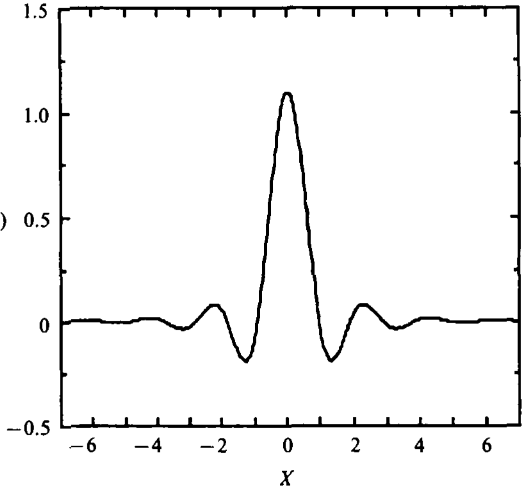

FIGURE 2. Smoothing function $\phi(x)$ that is orthonormal to the LMB wavelets. It also has exponential decay in physical space.

It also has the property that its translates are orthonormal to itself as well as to the wavelets ψ, but it is not orthogonal to its own dilations.

$$\int_{-\infty}^{\infty} \phi^{(m)}(x-2^m i)\,\psi^{(n)}(x-2^n j)\,\mathrm{d}x = 0, \tag{32}$$

$$\int_{-\infty}^{\infty} \phi^{(m)}(x-2^m i)\,\phi^{(m)}(x-2^n j)\,\mathrm{d}x = \delta_{ij}. \tag{33}$$

Figure 2 shows $\phi(x)$. Intuitively, the basis function $\Psi^{(m,q)}[\boldsymbol{x}-2^m \boldsymbol{i}]$ for $q=1$ picks up variations of scale 2^m that occur in all three directions (x_1, x_2, x_3) simultaneously, for $q=7$ it only picks up fluctuations along the direction x_3, etc. It can be proved that with a proper choice of both $\psi(x)$ and $\phi(x)$, one can represent a three-dimensional function $f(\boldsymbol{x})$ as

$$f(\boldsymbol{x}) = \sum_m \sum_{q=1}^{7} \sum_{(i_1,i_2,i_3)} w^{(m,q)}[i_1,i_2,i_3]\,\Psi^{(m,q)}[\boldsymbol{x}-2^m \boldsymbol{i}]. \tag{34}$$

Again, the coefficients can be computed as

$$w^{(m,q)}[i_1,i_2,i_3] = \int_{-\infty}^{\infty}\int_{-\infty}^{\infty}\int_{-\infty}^{\infty} f(\boldsymbol{x})\,\Psi^{(m,q)}[\boldsymbol{x}-2^m \boldsymbol{i}]\,\mathrm{d}x_1\,\mathrm{d}x_2\,\mathrm{d}x_3. \tag{35}$$

2.4. *Discrete wavelet transform*

Thus far we have considered continuous functions $f(x)$. For practical applications, it is important to have a discrete transform, because functions such as $f(x)$ will only be known on a discrete mesh x_j.

2.4.1. *One-dimensional case*

We consider a function $f(x)$ sampled on a discrete mesh, $f(x_j) = f[j]$, where $x_j = jh$ and h is the mesh spacing. The discrete analogue of (24) is

$$f[j] = \sum_{m=1}^{\infty} \sum_{i=-\infty}^{\infty} w^{(m)}[i]\,g^{(m)}[i-2^m j], \tag{36}$$

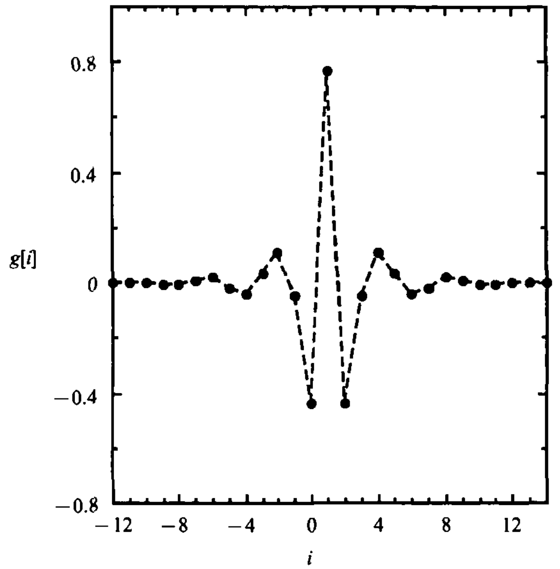

FIGURE 3. Discrete Lemarie–Meyer–Battle (LMB) wavelet.

where $g^{(m)}[i]$ is a discrete version of the wavelet function $\psi^{(m)}(x)$. The precise sense of 'discrete version' and how to compute $g^{(m)}[i]$ is explained in Appendix B of II, here we indicate only that $\psi(x)$ is sampled at discrete meshpoints using not δ-functions but rather the smoothing function $\phi(x)$ introduced above. Figure 3 shows $g^{(m)}[i]$ for $m = 1$ corresponding to the LMB wavelet. This function obeys the 'discrete orthogonality' condition

$$\sum_{k=-\infty}^{\infty} g^{(m)}[k-2^m i]\, g^{(n)}[k-2^n j] = \delta_{ij}\,\delta_{mn}. \tag{37}$$

The coefficients $w^{(m)}[i]$ are given by

$$w^{(m)}[i] = \sum_{j=-\infty}^{\infty} g^{(m)}[i-2^m j] f[j]. \tag{38}$$

These convolutions can be performed either in physical space or in Fourier space. If the support of $g[i]$ is small (i.e. it is non-zero on a few grid-points) it is more convenient to operate in physical space. If the support is not small (such as with the LMB wavelets which decay exponentially) one can perform the convolution in Fourier space using the FFT. Furthermore, the different levels m are handled in a recursive fashion, leading to the 'fast wavelet transform'. In practice one deals with finite domains so that the sums of (36) and (38) extend over N grid-points. In this work we will use periodicity when computing the convolutions via FFT; when the fields are not periodic, appropriate windowing is used. More details on all of these issues are given in Appendices A, B and C of II. The total energy obeys again

$$\sum_{j=-\infty}^{\infty} f[j]^2 = \sum_{m=1}^{\infty} \sum_{i=-\infty}^{\infty} (w^{(m)}[i])^2. \tag{39}$$

To illustrate the discrete wavelet transform, consider the function $f[j]$ of figure 4,

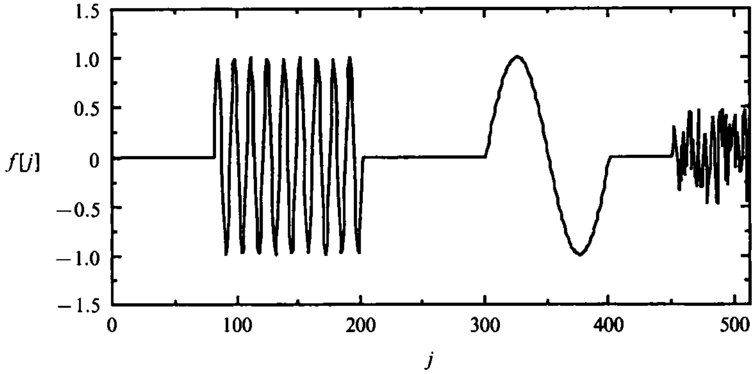

FIGURE 4. Illustrative example: function with regions of fluctuations of different wavelength and white noise at different locations.

with $N = 512$ grid-points. It exhibits localized oscillations at different scales and positions. To the right, it consists of white noise. Now we compute the transform by performing the convolutions of (38) using the LMB wavelet and the fast wavelet algorithm reviewed in Appendix B of II. The convolutions of (38) are computed with FFTs, assuming periodicity for the function $f[j]$ and using the fact that the wavelet $g^{(m)}[i]$ decays rapidly and is negligible at the boundaries (for the largest scales $m \sim \log_2(N)$ this is not true, but the errors are negligible: in this case the total energy of the signal and the wavelet coefficients were the same up to 11 significant digits).

Figure 5 shows the discrete coefficients, placed on a mesh of scale and position. There are $M = \log_2(N) = 9$ different values for m, and the transform is defined on $N/2^m$ positions at each level. Thus at large scales, the discretization is much coarser. Also, we remark that the total number of wavelet coefficients is

$$\sum_{m=1}^{M} \frac{N}{2^m} = N-1. \tag{40}$$

Additionally, one obtains a 'global DC offset' $s^{(M)}$ related to the mean of the signal (see Appendix B of II), so that information is conserved, as it should be for an orthonormal representation.

2.4.2. *Three-dimensional case*

In three dimensions we again need an additional function $h^{(m)}[j]$ which is the discrete version of $\phi^{(m)}(x)$. The decomposition is:

$$\begin{aligned} f[i_1,i_2,i_3] = \sum_{m=1}^{M} \Bigg\{ &\sum_{j_1,j_2,j_3} g^{(m)}[i_1-2^m j_1]\, g^{(m)}[i_2-2^m j_2]\, g^{(m)}[i_3-2^m j_3]\, w^{(m,1)}[j_1,j_2,j_3] + \dots \\ &+ \sum_{j_1,j_2,j_3} h^{(m)}[i_1-2^m j_1]\, h^{(m)}[i_2-2^m j_2]\, g^{(m)}[i_3-2^m j_3]\, w^{(m,7)}[j_1,j_2,j_3] \Bigg\}. \end{aligned} \tag{41}$$

The formula to obtain the coefficients is

$$w^{(m,q-1)}[i_1,i_2,i_3] = \sum_{j_1,j_2,j_3} q^{(m)}[i_1-2^m j_1]\, g^{(m)}[i_2-2^m j_2]\, g^{(m)}[i_3-2^m j_3]\, f[j_1,j_2,j_3], \tag{42}$$

and the other permutations of g and h yield all 7 coefficients for each scale m and location $[i_1, i_2, i_3]$. Because of separability into a product, the convolutions can be

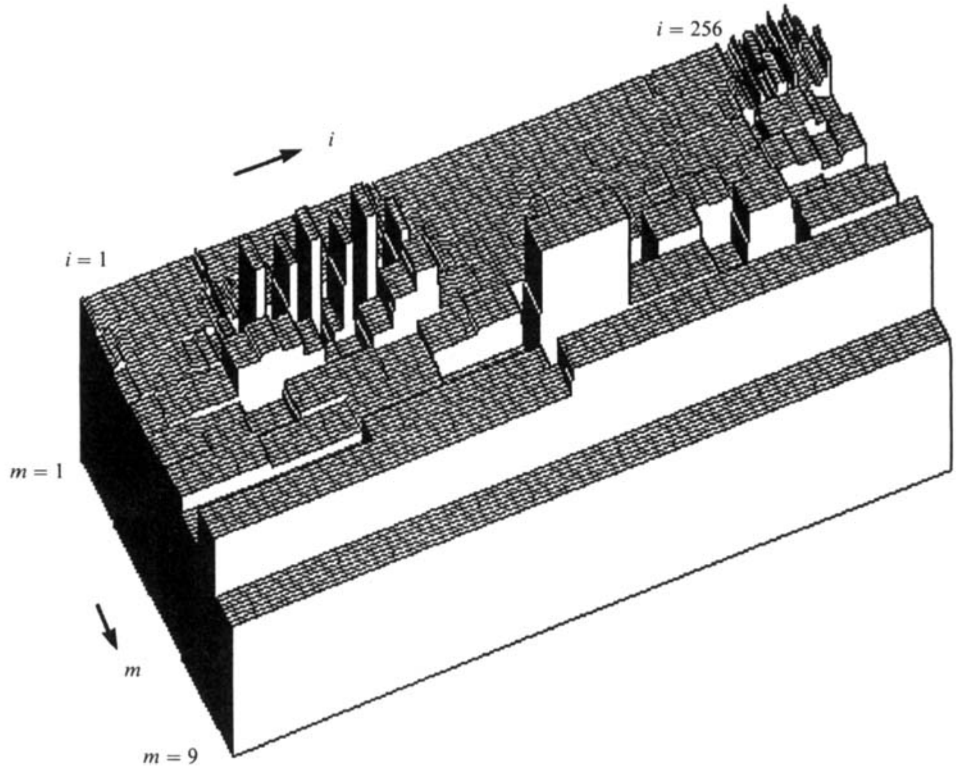

FIGURE 5. Discrete wavelet transform of the function in the preceding figure. The coefficients are defined on a grid becoming increasingly coarser at the larger scales. The coefficients are large at a scale corresponding to $m = 3$ and 4 (scales equal to 2^3 and 2^4) only near locations at the left, where the signal has oscillations of wavelength ≈ 12. Some leaking to other m bands is visible, owing to the finite bandwidth of the basis functions. The large-scale oscillation gives high coefficients at larger values of m while the white noise at the right produces non-zero coefficients at every scale on the right portion.

performed in succession along the three Cartesian coordinates. These convolutions can be performed either in physical space or in Fourier space. The total energy of the signal is given by summing over all scales m and components q:

$$\sum_{(i_1,i_2,i_3)} f[\boldsymbol{i}]^2 = \sum_{m=1}^{M} \sum_{q=1}^{7} \sum_{j_1,j_2,j_3} (w^{(m,q)}[\boldsymbol{j}])^2. \tag{43}$$

We now have the tools to efficiently compute the discrete wavelet transform of a field in one or three dimensions (if other dimensionalities are required, the formalism is easily extended). We can also invert the transform, and compute the energy of the signal using the wavelet representation. In the remainder of the paper, we use these tools to analyse turbulent velocity fields.

3. Navier–Stokes equations in wavelet space

Let us define $w_i(r, \boldsymbol{x})$ as the wavelet transform of the fluctuating part of the (divergence-free) velocity field $u_i(\boldsymbol{x})$. In vector notation this will be denoted as $\boldsymbol{w}(r, \boldsymbol{x})$ (these variables obviously also depend on time, which is omitted from here on for notational simplicity). From (20) it follows that $\boldsymbol{w}(r, \boldsymbol{x})$ is divergence-free.

Applying (18) to the Fourier-transformed Navier–Stokes equations (equation (2)), where the velocities on the right-hand side have been replaced by the inverse transform of $w_i(r, \boldsymbol{x})$, one obtains the evolution equation for $w_i(r, \boldsymbol{x})$:

$$\left(\frac{\partial}{\partial t} - \nu \nabla^2\right)[w_i(r, \boldsymbol{x})] = (2\pi C_\psi)^{-\frac{3}{2}} \int_{r'} \int_{r''} \int_{x'} \int_{x''} w_j(r', \boldsymbol{x}')\, w_k(r'', \boldsymbol{x}'')\, I_{ijk}(r, \boldsymbol{x}; r', r'', \boldsymbol{x}', \boldsymbol{x}'') \times \frac{\mathrm{d}r'\,\mathrm{d}r''\,\mathrm{d}^3\boldsymbol{x}'\,\mathrm{d}^3\boldsymbol{x}''}{r'^4 r''^4}, \quad (44)$$

where

$$I_{ijk}(r, \boldsymbol{x}; r', r'', \boldsymbol{x}', \boldsymbol{x}'') = (-i)\,(rr'r'')^{\frac{3}{2}} \int_{k} \int_{q} k_k P_{ij}(\boldsymbol{k})\, \hat{\psi}(r\boldsymbol{k})^*\, \hat{\psi}(r'\boldsymbol{q})\, \hat{\psi}[r''(\boldsymbol{k}-\boldsymbol{q})] \times \exp\left(\mathrm{i}[\boldsymbol{k}\cdot(\boldsymbol{x}-\boldsymbol{x}'') + \boldsymbol{q}\cdot(\boldsymbol{x}''-\boldsymbol{x}')]\right) \mathrm{d}^3\boldsymbol{q}\,\mathrm{d}^3\boldsymbol{k}. \quad (45)$$

Multiplication by $w_i(r, \boldsymbol{x})$ and adding over the components i yields the equation for the local energy:

$$\frac{\partial}{\partial t} e(r, \boldsymbol{x}) = t(r, \boldsymbol{x}) - \epsilon(r, \boldsymbol{x}) + \nu \frac{\partial}{\partial x_j}\left[w_i\left(\frac{\partial w_i}{\partial x_j} + \frac{\partial w_j}{\partial x_i}\right)\right], \quad (46)$$

where
$$e(r, \boldsymbol{x}) = \frac{1}{2} \sum_{i=1}^{3} [w_i(r, \boldsymbol{x})]^2, \quad (47)$$

is the local density of kinetic energy at scale r, and

$$t(r, \boldsymbol{x}) = \int\!\!\int\!\!\int\!\!\int w_i(r, \boldsymbol{x})\, w_j(r', \boldsymbol{x}')\, w_k(r'', \boldsymbol{x}'')\, I_{ijk}(r, \boldsymbol{x}; r', r'', \boldsymbol{x}', \boldsymbol{x}'') \frac{\mathrm{d}r'\,\mathrm{d}r''\,\mathrm{d}^3\boldsymbol{x}'\,\mathrm{d}^3\boldsymbol{x}''}{r'^4 r''^4} \quad (48)$$

is the local transfer of kinetic energy to scale r at location $\boldsymbol{x}$. This term exhibits interactions among triads of scales (r, r', r''), as well as interactions among triads of locations $(\boldsymbol{x}, \boldsymbol{x}', \boldsymbol{x}'')$. In (46), $\epsilon(r, \boldsymbol{x})$ is the energy dissipation incurred by scales of size r, and is given by

$$\epsilon(r, \boldsymbol{x}) = \nu \frac{\partial w_i}{\partial x_j}\left[\frac{\partial w_i}{\partial x_j} + \frac{\partial w_j}{\partial x_i}\right]. \quad (49)$$

Because of (10), the transfer conserves energy

$$\int_r \int_x t(r, \boldsymbol{x}) \frac{\mathrm{d}r\,\mathrm{d}^3\boldsymbol{x}}{r^4} = 0. \quad (50)$$

The flux of kinetic energy through scale r at location $\boldsymbol{x}$ is defined by integrating the rate of change in the local energy due to nonlinear interactions over all scales larger than r,

$$\pi(r, \boldsymbol{x}) = -\int_r^\infty t(r', \boldsymbol{x}) \frac{\mathrm{d}r'}{r'^4}. \quad (51)$$

This is defined as usual with a negative sign, so that a decrease in energy of the large scales corresponds to a positive flux. This quantity is analogous to (4) in the wavelet representation, and because of (50) we have the condition

$$\lim_{r\to 0} \int_x \pi(r, \boldsymbol{x})\,\mathrm{d}^3\boldsymbol{x} = 0. \quad (52)$$

These formal expressions are not very useful in themselves, but they illustrate that there are complicated interactions of the $w_i(r, \boldsymbol{x})$ occurring at different positions as well as at different scales. These non-local and inter-scale interactions are controlled by the properties of $I_{ijk}(r, \boldsymbol{x}; r', r'', \boldsymbol{x}', \boldsymbol{x}'')$. We note that the complexity of this quantity stems primarily from the fact that in general the triads are not closed as they are in the Fourier case, i.e. there is no detailed energy conservation in the wavelet representation.

Further development of this formulation should concentrate on possible approximations to $I_{ijk}(r, \boldsymbol{x}; r', r'', \boldsymbol{x}', \boldsymbol{x}'')$ in order to simplify the nonlinear interactions (see Nakano 1988). In this paper we concentrate instead on analysis of actual turbulent flows and will make no approximations at this stage. When the velocity field is known, we can compute quantities such as $e(r, \boldsymbol{x})$, $t(r, \boldsymbol{x})$ and $\pi(r, \boldsymbol{x})$ by taking the wavelet transform of the Navier–Stokes equation with the nonlinear terms written as a function of the original velocity field. Also, as outlined in §2, we will use the discrete formulation, which is presented below.

We return to the Navier–Stokes equations written in physical space for the fluctuating velocity and pressure, (1). Let $w_i^{(m,q)}[\boldsymbol{i}]$ be the wavelet coefficient of the ith component of the velocity field, where $\boldsymbol{i} = (i_1, i_2, i_3)$ denotes location on a rectangular grid with constant mesh-sizes h_1, h_2, h_3. This location will be given by $\boldsymbol{y} = 2^m(h_1 i_1, h_2 i_2, h_3 i_3)$. We then have

$$w_i^{(m,q)}[\boldsymbol{i}] = \int_{-\infty}^{\infty}\int_{-\infty}^{\infty}\int_{-\infty}^{\infty} u_i(\boldsymbol{x})\, \Psi^{(m,q)}[\boldsymbol{x}-\boldsymbol{y}]\, \mathrm{d}x_1\, \mathrm{d}x_2\, \mathrm{d}x_3. \tag{53}$$

Now we take the inner product of the Navier–Stokes equation with the wavelet basis function $\Psi^{(m,q)}(\boldsymbol{x}-\boldsymbol{y})$. Also, as a short notation, the coefficients of the terms other than velocity will be denoted by enclosing them in brackets like $\{\ldots\}^{(m,q)}[\boldsymbol{i}]$. Therefore, we write

$$\frac{\partial}{\partial t} w_i^{(m,q)}[\boldsymbol{i}] = -\left\{u_j \frac{\partial u_i}{\partial x_j} + \frac{1}{\rho}\frac{\partial p}{\partial x_i}\right\}^{(m,q)}[\boldsymbol{i}] + \{\nu \nabla^2 u_i\}^{(m,q)}[\boldsymbol{i}]. \tag{54}$$

Multiplication by $w_i^{(m,q)}[\boldsymbol{i}]$ and contraction over the three components i and seven terms q yields the evolution equation for the local kinetic energy density $e^{(m)}[\boldsymbol{i}]$, of scale r_m and location $\boldsymbol{y} = 2^m(h_1 i_1, h_2 i_2, h_3 i_3)$:

$$\frac{\partial}{\partial t} e^{(m)}[\boldsymbol{i}] = t^{(m)}[\boldsymbol{i}] - v^{(m)}[\boldsymbol{i}]. \tag{55}$$

This equation is analogous to (3), but it depends on position as well. Here $t^{(m)}[\boldsymbol{i}]$ is the local transfer of kinetic energy to scales r_m at location indexed by $\boldsymbol{i}$, which is given by

$$t^{(m)}[\boldsymbol{i}] = -\sum_{i=1}^{3}\sum_{q=1}^{7} w_i^{(m,q)}[\boldsymbol{i}]\left\{u_j \frac{\partial u_i}{\partial x_j} + \frac{1}{\rho}\frac{\partial p}{\partial x_i}\right\}^{(m,q)}[\boldsymbol{i}]. \tag{56}$$

The pressure appearing in this definition need not be the total pressure, but is the one that arises from solving the Poisson equation, the source term including only the fluctuating part of the velocity and not the mean speed (for more details, see §5.2). $v^{(m)}[\boldsymbol{i}]$ is the viscous term (containing dissipation and viscous transport of kinetic energy), and is given by

$$v^{(m)}[\boldsymbol{i}] = \nu \sum_{i=1}^{3}\sum_{q=1}^{7} w_i^{(m,q)}[\boldsymbol{i}]\{-\nabla^2 u_i\}^{(m,q)}[\boldsymbol{i}]. \tag{57}$$

We focus attention on the nonlinear term $t^{(m)}[\boldsymbol{i}]$, which indicates how the kinetic energy is transferred by the nonlinear interactions, among the different scales and locations. This term conserves energy on the whole:

$$\sum_{m=1}^{M} \sum_{i_1, i_2, i_3} t^{(m)}[i_1, i_2, i_3] = 0, \tag{58}$$

a property that follows from the condition that the volume integral of $\boldsymbol{u}\cdot\nabla\boldsymbol{u}+\nabla p$ is zero (for homogeneous turbulence), and from the orthonormality of the wavelets.

In analogy to (4), the flux of kinetic energy through a spatial region of characteristic size r_m and location given by the index $[i_1, i_2, i_3]$ can be computed by adding the transfer (density) of all larger scales at that location, according to

$$\pi^{(m)}[\boldsymbol{i}] = -\sum_{n=m}^{M} 2^{3(M-n)} t^{(n)}[2^{m-n}\boldsymbol{i}]. \tag{59}$$

It is the quantities $e^{(m)}[\boldsymbol{i}]$, $t^{(m)}[\boldsymbol{i}]$ and $\pi^{(m)}[\boldsymbol{i}]$ that we wish to measure in turbulent flows. The next section focuses on the energy itself; one part of it can be measured for the laboratory flows, while in three-dimensional direct numerical simulations it can be measured in its entirety.

4. Spatial statistics of turbulent kinetic energy

The purpose of this section is the measurement and characterization of the local kinetic energy at every scale in turbulent flows. Before describing the actual measurements, we introduce a few tools that will be used, and highlight their connection with the usual Fourier analysis.

4.1. *Basic concepts*

In Fourier analysis, the tools often used to characterize a process are correlation functions or the power-spectral density $E(k)$ that represent the energy-density contained in a band $\mathrm{d}k$ of wavenumbers, and thus provides a measure of the relevance of each scale of motion. However, important spatial information is lost owing to the non-local nature of the Fourier modes. We will relate the wavelet energies with $E(k)$, and use them to quantify the spatial distribution of the energy in more complete statistical terms.

Let $u(x)$ be a one-dimensional finite-energy function of zero mean, and let $\hat{u}(k)$ be its Fourier transform. The total energy is given by

$$\int_{-\infty}^{\infty} u(x)^2\,\mathrm{d}x = \frac{1}{2\pi}\int_{-\infty}^{\infty} \hat{u}(k)\,\hat{u}(k)^*\,\mathrm{d}k = \int_0^{\infty} E(k)\,\mathrm{d}k, \tag{60}$$

where $E(k)$ is the energy spectrum. The wavenumber k in Fourier space is related to physical distances r by

$$k = \frac{2\pi}{r}. \tag{61}$$

Let $w(r,x)$ be the continuous wavelet transform of $u(x)$. From (10) and (61), the total energy can be written in terms of the wavelet energies as

$$\int_{-\infty}^{\infty} u(x)^2\,\mathrm{d}x = \int_0^{\infty} E_w(k)\,\mathrm{d}k, \tag{62}$$

where
$$E_w(k) = \frac{1}{2\pi} C_\psi^{-1} \int_{-\infty}^{\infty} w(r(k), x)^2 \, \mathrm{d}x. \tag{63}$$

This is the energy-density at wavenumbers k obtained from the wavelet coefficients. This spectrum is analogous to the Fourier spectrum $E(k)$, but need not be exactly the same at every k because of the finite bandwidth associated with the wavelet transform. Before averaging in physical space, we can perform other statistical calculations that will reveal more detailed information about $u(x)$. For instance, we can inquire about deviations from Gaussian behaviour at every scale by computing the skewness and flatness factors of $w(r, x)$. The flatness factor is given by

$$F(k) = \frac{\langle w[r(k), x]^4 \rangle}{\langle w[r(k), x]^2 \rangle^2}, \tag{64}$$

where the averaging is performed over x.

In the discrete case, we consider $w^{(m)}[i]$, the discrete wavelet coefficients of the velocity field:

$$w^{(m)}[i] = \int_{-\infty}^{\infty} u(x)\, \psi^{(m)}(x - 2^m i)\, \mathrm{d}x. \tag{65}$$

When $u(x)$ is represented as $u[j]$ on a finite domain on N gridpoints, we compute

$$w^{(m)}[i] = \sum_{j=1}^{N} u[j]\, g^{(m)}[j - 2^m i], \tag{66}$$

where $N = 2^M$. From (28), the total energy density contained in scales $r_m = 2^m h$ is given by

$$N^{-1} \sum_{j=1}^{2^{M-m}} (w^{(m)}[j])^2. \tag{67}$$

The wavenumber corresponding to this scale is

$$k_m = \frac{2\pi}{r_m} = 2\pi 2^{-m} h^{-1}. \tag{68}$$

The power-spectral density (per unit wavenumber) is expression (67) divided by Δk_m. From (68) it follows that $\Delta k_m = 2\pi 2^{-m} h^{-1} \ln 2$. Finally, the power-spectral density corresponding to k_m will be given by

$$E(k_m) = \langle (w^{(m)}[j])^2 \rangle \frac{h}{2\pi \ln(2)}, \tag{69}$$

where the average is a spatial one over all j locations at scale corresponding to k_m. Notice however that the resolution in terms of scales is considerably less dense than in the case of the Fourier spectral density: there we have information at wavenumbers spaced linearly, here we obtain that information only on octaves. However, in addition to the energy spectral density, we can inquire about deviations of the energy about its mean $\langle (w^{(m)}[j])^2 \rangle$ or $E(k_m)$. This can be quantified by the variance of $(w^{(m)}[j])^2$, which is essentially a fourth-order moment of the wavelet coefficient. The standard deviation of energy is

$$\sigma_E(k_m) = \frac{h}{2\pi \ln(2)} [\langle (w^{(m)}[j])^4 \rangle - \langle (w^{(m)}[j])^2 \rangle^2]^{\frac{1}{2}}. \tag{70}$$

This is a measure of the spatial fluctuations of the localized energy contributions, in the same units as $E(k_m)$. A plot of $E(k_m)$ as well as of $E(k_m)+\sigma_E(k_m)$ gives a compact representation of the energy contained in each scale and its spatial variability. We will refer to such a representation as the 'dual spectrum' of a signal, and will use this and similar tools frequently throughout this paper.

Furthermore, the flatness factor is given by

$$F(k_m) = \frac{\langle w^{(m)}[j]^4\rangle}{\langle w^{(m)}[j]^2\rangle^2}. \tag{71}$$

Here again the averaging is over all j-locations at a given scale and we use the property that the mean of the wavelet coefficients is zero for each scale. We believe that such quantities can give useful insight about the spatial properties of turbulence in a compact statistical fashion, at every scale of motion. Furthermore, we stress that the calculations can be made at a similar cost to the usual FFT analysis.

In practice, the scale range of interest does not need to extend to scales as large as the total length of the signal. In such a case one can compute the transform over segments of the signal and then average over them. As when computing Fourier spectra, certain windowing procedures must be used. The details of this are given in Appendix C of II.

In three dimensions, we use the wavelet coefficient of the ith velocity component, $w_i^{(m,q)}[\boldsymbol{i}]$ (see (53)). The energy spectral tensor of the velocity field $\boldsymbol{u}$ is

$$E_{ij}(k_m) = \frac{2^{-2m}(h_1 h_2 h_3)^{\frac{1}{3}}}{2\pi \ln(2)}\langle e_{ij}^{(m)}[\boldsymbol{i}]\rangle, \tag{72}$$

where the average extends over all points $[\boldsymbol{i}]$, and we have defined

$$e_{ij}^{(m)}[\boldsymbol{i}] = \frac{1}{2}\sum_{q=1}^{7} w_i^{(m,q)}[\boldsymbol{i}]\, w_j^{(m,q)}[\boldsymbol{i}]. \tag{73}$$

In (72), we have accounted for possibly, non-equal mesh-sizes in each direction by taking the characteristic scale as the geometric mean,

$$r_m = 2^m (h_1 h_2 h_3)^{\frac{1}{3}}. \tag{74}$$

The total kinetic energy (per unit volume) of the field is given by

$$\tfrac{1}{2}q^2 = \sum_{i=1}^{3}\sum_{m=1}^{M} \Delta k_m E_{ii}(k_m). \tag{75}$$

The spectral tensor $E_{ij}(k_m)$ is analogous to the radial energy spectrum tensor $E_{ij}(k)$ from Fourier analysis, but is not necessarily equal to it at every k because of the width of the Fourier transform of the wavelet. The spatial variation of $e_{ij}^{(m)}[\boldsymbol{i}]$ is measured by its standard deviation in units of $E_{ij}(k_m)$ as

$$\sigma_{ij(E)}(k_m) = \frac{2^{-2m}(h_1 h_2 h_3)^{\frac{1}{3}}}{2\pi \ln(2)}[\langle [e_{ij}^{(m)}]^2\rangle - \langle e_{ij}^{(m)}\rangle^2]^{\frac{1}{2}}. \tag{76}$$

The three-dimensional dual energy spectra will be given by the traces of these tensors. The skewness and flatness factors can be determined by spatial averages over all points, and one can define different factors for each velocity component, as well as for each term $q = 1, \ldots, 7$.

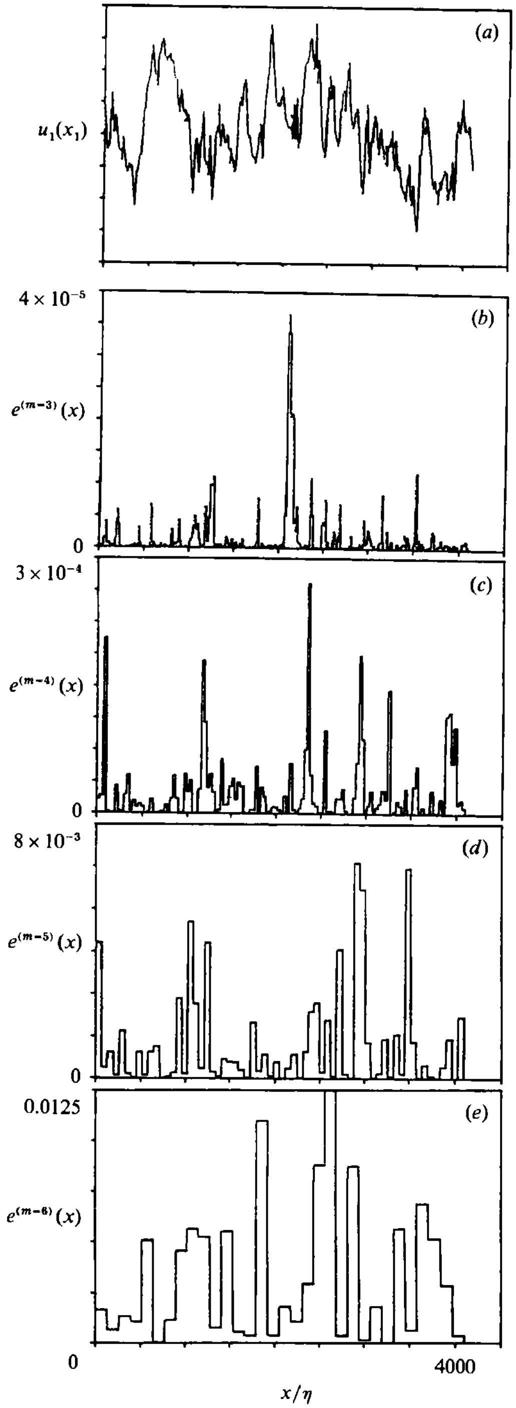

FIGURE 6. (*a*) Streamwise velocity signal measured in the wake of a circular cylinder, as a function of streamwise position (Taylor's hypothesis has been used). (*b*)–(*e*) Energies of the velocity at different locations and different scales of motion (the energy is plotted in arbitrary units). The energy increases at the large scales, but large fluctuations in physical space are visible at every scale of motion.

In the remainder of this paper we will use the scale r_m, wavenumber k_m or the index m to denote the size of the wavelet in an interchangeable fashion.

4.2. *Applications to laboratory measurements*

In this section we compute the dual spectra of two experimental data sets consisting of records of streamwise velocity component. The flows considered are a turbulent boundary layer and the turbulent wake behind a circular cylinder.

The experimental velocity fields have been obtained in a suction wind-tunnel (at Yale University) using a single-point hot-wire anemometer. Details of the measurements can be found in I. The boundary-layer flow has a free-stream velocity of 12 m/s, the hot wire is located at $y/\delta = 0.2$ (where the boundary-layer thickness is $\delta \approx 4$ cm), and the Taylor micro-scale Reynolds number is $Re_\lambda = 110$. The turbulent wake flow has a free-stream velocity of 9 m/s, the measuring station is in the centreline at $x/d = 90$, where $d = 1.9$ cm is the cylinder diameter. The Reynolds number is $Re_\lambda = 50$. For both experiments, the turbulence intensity is low (5 and 3.6%) compared to the convecting mean speed, and Taylor's hypothesis has been used in interpreting the data sets as linear sections through a 'frozen' flow field. Digitizer noise from the 12 bit analogue-to-digital converter was eliminated by passing the signal through a low-pass filter with a cutoff frequency of $k\eta = 1$ using a digital filter of approximately 100 dB/octave. This affects only the smallest scales (corresponding to 5 grid-points or less), which are much smaller than those at the peak of the dissipation spectrum.

For the remainder of this section we consider the spatial statistics of the turbulent kinetic energy. A portion of the velocity signal consisting of 2^{11} points, obtained in the turbulent wake is shown in figure 6(*a*). We compute the one-dimensional wavelet transform of this velocity signal (using the LMB wavelet basis) with $M = 12$ scales with the windowing procedure described in Appendix C of II. We then determine the local energies at every location in the flat part of the window. In figure 6(*b*–*e*) we show the spatial distribution of energy for 4 scales, $m = 3$ to $m = 6$. It is quite evident that the magnitude of the energy becomes smaller at smaller scales in accordance with the spectrum of the signal. The degree of intermittency or spottiness increases at smaller scales however. These spotty regions are located near sharp jumps in the velocity signal. Intermittent signals like figure 6(*b*) have often been observed when measuring small-scale quantities like rates of energy dissipation. Here, on the contrary, we are dealing with intermediate scales which are dynamically quite important.

The dual energy spectra are obtained by averaging over many segments of data, in each of which the appropriate windowing method is used. We compute the wavelet transform with $M = 12$ for 100 segments and perform the average of (69) over them for proper statistical convergence of the spectrum. In figure 7, we show the dual spectra of the one-dimensional signals, compared with the usual Fourier power-spectrum (solid line). The mean wavelet spectrum agrees fairly well with the Fourier spectrum at the large scales. At the small scales, the spectrum becomes very steep and there is a significant difference. This is due to the tail of the wavelet in Fourier space, which generates some 'leaking' of energy from the large scales to the small ones. Of course, there is no 'true' energy spectrum *per se*, the wavelet spectrum just corresponds to the actual energy contained in pulses rather than in waves. The only condition that must be met by both spectra is that the total energy be the same, and this was checked here to be true up to roundoff accuracy.

The variance of the energy provides additional information, and for most of the

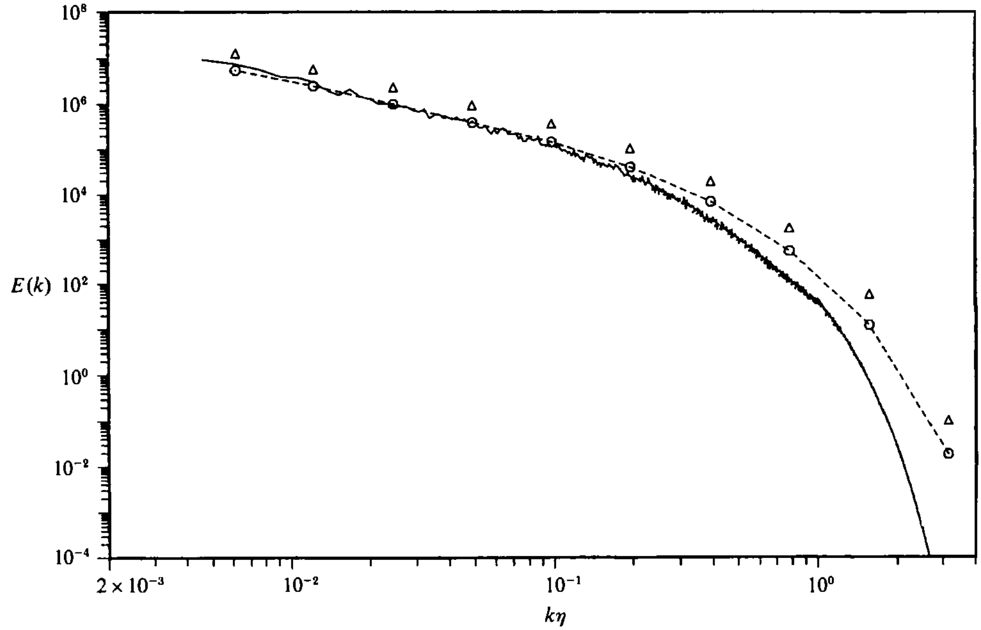

FIGURE 7. Dual energy spectrum of the turbulent flow behind the circular cylinder (streamwise one-dimensional spectrum). ——, Usual Fourier spectrum; ○, wavelet spectrum; △, wavelet mean energy at every scale to which one standard deviation (computed from the spatial fluctuations) has been added.

scales it is of the same order of magnitude as the mean energy itself. The small increase in the relative variance of the local energies at large wavenumbers points to an increasingly intermittent distribution of the kinetic energy there. This behaviour cannot be detected with the usual Fourier spectra. This can be seen more dramatically in the plot of the flatness factor $F(k_m)$ as a function of k in figure 8, which includes the results for the boundary layer as well as those of the turbulent wake. For both flows $F(k_m)$ increases steadily from the Gaussian value 3 at the large scales through the intermediate ones, and increases more quickly in the dissipative range.

4.3. *Multifractal nature of local kinetic energy*

Traditionally, less attention has been given to the intermittent nature of the energy than to that of the dissipation because the average of the energy is dominated by the large scales of the flow, and thus small-scale intermittency is less relevant. However, intermittent behaviour of the local energy is present at all intermediate scales and may be quite relevant for the formulation of turbulence models. We will analyse the possibility that the quantity $e(r,x) = w(r,x)^2$ may behave as a multifractal field (measure). For accounts of the multifractal formalism see Mandelbrot (1974), Parisi & Frisch (1985) and I.

If $e^{(m)}[j]$ is multifractal (this discussion is made in terms of the discrete transform but can also be made in the continuous version), one can define a set of scaling exponents D'_q for the qth moment by

$$\langle (e^{(m)}[j])^q \rangle \sim \langle e^{(m)}[j] \rangle^q \left(\frac{r_m}{L}\right)^{(q-1)(D'_q-d)}. \tag{77}$$

D'_q are the so-called 'generalized dimensions' of the energy which describe the scaling

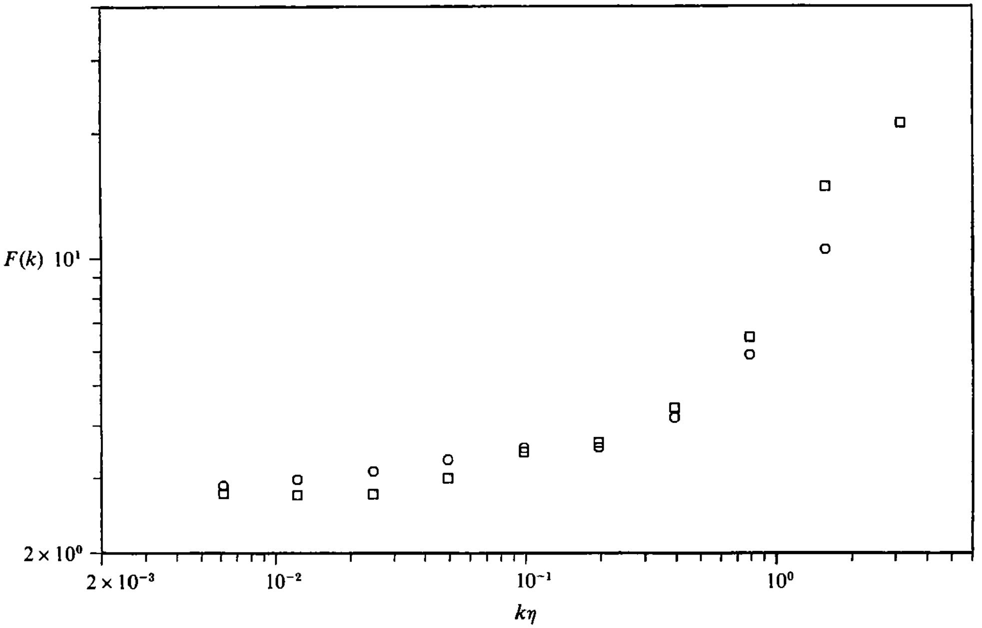

FIGURE 8. Flatness factors of the wavelet coefficient computed from laboratory data. The circles are for the boundary-layer flow and the squares are for the turbulent wake.

of moments of order q of the field (there is no connection between this q and the index used in the preceding chapters to denote different terms in the multidimensional orthonormal wavelet analysis). Also, d is the dimension of the embedding space ($d = 1$ for the experimental data). The prime indicates that these exponents refer to the local energies rather than to the dissipation as introduced in Meneveau & Sreenivasan (1987*a*). Alternatively, one can locally define a scaling exponent α' as

$$e^{(m)}[i] \sim \langle e^{(m)}[j] \rangle \left(\frac{r_m}{L} \right)^{\alpha' - d} \tag{78}$$

whose probability density function $P_m(\alpha')$ scales as

$$P_m(\alpha') \sim \left(\frac{r_m}{L} \right)^{d - f'(\alpha')}. \tag{79}$$

Here $f'(\alpha')$ is a scale-invariant function (called the multifractal spectrum) when the field is multifractal. The generalized dimensions and the function $f'(\alpha')$ can be related by

$$\alpha'(q) = \frac{\mathrm{d}}{\mathrm{d}q}(q-1)D'_q, \tag{80}$$

$$f'(\alpha') = q\alpha'(q) - (q-1)D'_q. \tag{81}$$

It is important to note a fundamental difference between the definitions used here and the multifractal formalism commonly employed for conservative measures (such as the dissipation or invariant measures in dynamical systems). There one deals with 'conservative cascades' (see the discussion in I), where the integral or sum of the field is a value independent of the scale r. When dealing with the dissipation, this constant value is the overall mean rate of dissipation, and is usually thought to be

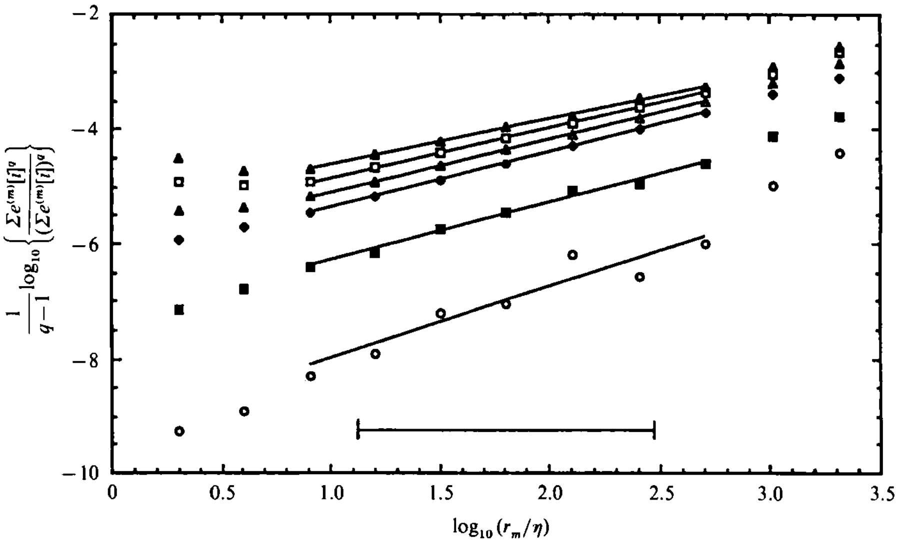

FIGURE 9. Double logarithmic plots of the properly normalized q-sums of the wavelet energies for the laboratory boundary layer. Linear portions for positive q values are clearly visible between scales $m = 4$ and $m = 8$ ($r_m/\eta \sim 20$ and $r_m/\eta \sim 200$). For smaller scales, there is a clear levelling of the curves, and for larger scales, the slopes increase to the space-filling value 1. For negative q, the scatter of the points is very large, even using this many points. The solid lines whose slopes are used to obtain the D'_q exponents are least-square fits to the points in the scaling range.

representative of the net flux of kinetic energy from large to small scales, independent of scale in the inertial range. Thus the prefactor in the right-hand side of (77) is usually independent of r (or m). Here, however, the total kinetic energy at some particular scale is not a constant and its dependence on scale is given by the energy spectrum. As in the previous section, the present multifractal formalism is a means of characterizing the intermittency of the energy distribution around its scale-dependent mean. Definition (77) is more closely related to the multifractal formalism introduced in Parisi & Frisch (1985) for velocity structure functions (of even order). The analogy is due to a close (but not exact) resemblance of wavelet coefficients of a certain scale with velocity increments over such a scale, which we shall exploit later to relate the appropriate exponents. For additional information on the relation between multifractals and wavelets, see Arneodo, Grasseau & Holschneider (1988) and Barcy *et al.* (1990).

In practice, the exponents D'_q can be measured from log–log plots of

$$\{\sum_j (e^{(m)}[j])^q (\sum_j e^{(m)}[j])^{-q}\}^{1/(q-1)} \tag{82}$$

versus (r_m/L) as the slope of a linear region (if it exists) somewhere between the energy-containing scales and the dissipative ones. By ergodicity, the ensemble averaging of (77) is replaced by sums over all j indices, but we emphasize that the calculations of (82) are closely related to the evaluation of structure functions (of even order $p = 2q$). To obtain the multifractal spectrum, we then apply (80) and (81).

Thus we proceed as follows: divide the signal into segments of 2048 points and multiply the data by the window described in Appendix C of II. The wavelet coefficients are computed for each segment with $M' = 12 = M+1$. Then the sums implied by (82) are computed for every r or m value ($m = 1, 2, \ldots, M$) and for 19

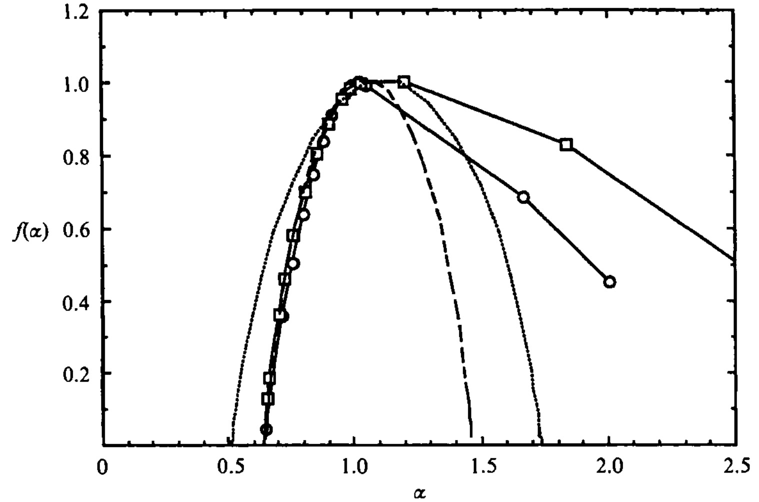

FIGURE 10. Singularity spectra for one-dimensional cuts through turbulence. The symbols are the present results from the local kinetic energies (squares for the wake flow and circles for the boundary layer). ...., Mean $f(\alpha)$ curve of the field of dissipation obtained previously (see I) from a variety of turbulent shear flows; ---, $f(\alpha)$ of the energies deduced from the $f(\alpha)$ curve of the dissipation using the usual (local) dimensional analysis. There is excellent agreement with the values directly measured (symbols) on the left-hand side but no agreement on the right-hand side.

values of q, between $q = -3$ and $q = 6$. The sums extend only over those j-values within the flat part of the window. To guarantee statistical convergence for the high moments, very long segments of data were employed (2.5×10^6 points).

This analysis is performed for both the boundary-layer and the wake flow. Figure 9 shows log–log plots obtained in the boundary layer, which display an approximately linear portion for the decade of scales between $r_m/\eta_K \approx 20$ and $r_m/\eta_K \approx 200$ for the different q-values. This is the same scaling range found for this flow in I from analysis of the multifractal properties of the dissipation field. The same result is observed for the wake flow. The slopes are computed from least-square error fits to the 5 points from $m = 4$ to $m = 8$. Figure 10 shows the $f(\alpha)$ curve obtained after application of (80) and (81) to the D'_q curve. In this plot, we also show the $f(\alpha)$ curve obtained in I for the dissipation field (dotted line). We note that $\alpha'_{\min}$ is larger than $\alpha_{\min}$ of the dissipation, indicating that the energy is less intermittent than the dissipation. There is a large qualitative difference on the right part of $f(\alpha)$, corresponding to the low-intensity regions (this can also be seen in the sharp increase in the D_q curve at negative q values). While the dissipation is reasonably well behaved here (the curve drops continuously to low values), the curves corresponding to the local energy seem to level off at a certain (negative) slope. This behaviour is indicative of a fundamental change in the distribution (analogous to a phase transition, Min Duong-van 1987). This is due to the fact that the probability density of the local energies peaks at zero energy, which differs in a fundamental way from the behaviour of the (coarse-grained) dissipation whose distribution function vanishes at small dissipation values. This means that negative moments of the energy (based on a single velocity component – when adding three components the situation would change) do not exist or are ill-behaved if one attempts to compute them (a similar conclusion is reached in Bacry *et al.* (1990), where it is argued that the negative moments of velocity differences could not scale in the same fashion as those of the dissipation).

An interesting question is whether the present results can be related to the $f(\alpha)$ curve of the dissipation through dimensional analysis. In Meneveau & Sreenivasan (1987*a*, 1991) it has been shown that such a relationship works for the scaling of positive even moments of velocity structure functions. The usual assumption is that velocity differences $\Delta u_r(x)^2 = [u(x+r)-u(x)]^2$ scale in the same fashion as $(r\epsilon_r(x))^{\frac{2}{3}}$, where ϵ_r is the dissipation of kinetic energy averaged over a box of linear size r. From dimensional analysis, one expects that $(\Delta u_r)^2 \sim kE(k)$, which leads to

$$e^{(m)}[j] \sim \left(\frac{r_m}{L}\right)^d [r_m \, \epsilon_{r_m}(x_j)]^{\frac{2}{3}} \tag{83}$$

locally. This can be used to obtain the following relation:

$$D'_q = D_{\frac{2}{3}q} + \frac{q}{3(q-1)}(D_{\frac{2}{3}} - D_{\frac{2}{3}q}), \tag{84}$$

where D_q are the generalized dimensions of the dissipation field. Applying this equation to the mean D_q curve for the dissipation obtained in I, and then transforming to the $f(\alpha)$ representation, we obtain the dashed line of figure 10. The agreement is good on the left-hand part of the curve, but as expected from the discussion above, there is no agreement on the low-intensity part. This means that (83) is not valid for low values of dissipation and energy.

4.4. *Analysis of three-dimensional numerically generated fields*

We now turn to the statistics of energy from three-dimensional velocity fields. One flow considered is a freely decaying isotropic turbulent field with periodic boundary conditions, obtained using the pseudospectral method (see Rogallo 1982). The field was initialized with Fourier modes with a prescribed energy spectrum and random phases. The calculation was performed for a sufficiently long time to establish the nonlinear interactions and a velocity derivative skewness $S = -0.51$. The computational grid-size was 120^3 (expanded during post-processing to 128^3 for the analysis in physical space by zero-padding in Fourier space). The Taylor-scale Reynolds number is about $R_\lambda = 30$.

The other flow field considered is a simulation of homogeneous sheared turbulence, described in detail in Rogers, Moin & Reynolds (1976) and Rogers & Moin (1986). Here we consider the field C128U12, computed on a 128^3 grid using Rogallo's (1982) deforming grid algorithm, in which periodic boundary conditions can be used. The field at a time equal to 12 shear timescales ($St = 12$) was analysed. The turbulence field is homogeneous in all spatial directions, but is not isotropic. Elongated vortical structures are visible. The Taylor-scale Reynolds number Re_λ is 110, where λ is defined using the streamwise velocity and streamwise velocity gradient (it is thus higher than the equivalent isotropic scale). The physical grid spacing for this computation is twice as large in the x-(streamwise) direction as in the other two directions.

We compute the three-dimensional wavelet transform of the three velocity components according to the procedure of §2.4.2, again using the LMB wavelet basis. Because the fields are periodic no windowing of the data is needed, but because of the elongation of the grid in the x-direction, the actual wavelet basis functions are twice as long in that direction as in the transverse directions. This is quite appropriate for

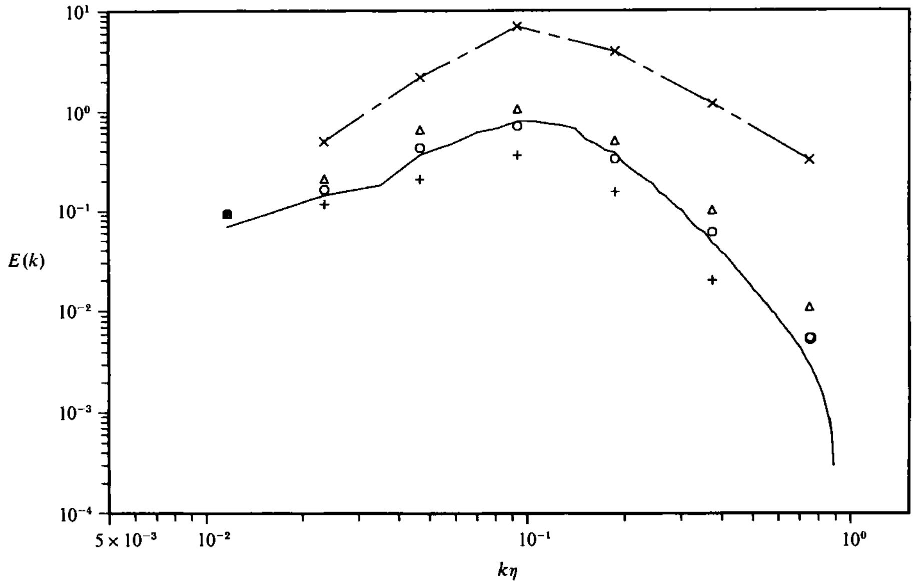

FIGURE 11. Dual spectrum of the homogeneous shear flow. These are total spectra (sum over all three velocity components). —, Usual (radial) Fourier spectrum; ○, wavelet spectrum; △ and +, mean spectrum plus and minus the standard deviation of the spatial fluctuations of the energies at every scale. The × correspond to the maximum spatial energy occurring at every scale.

a non-isotropic flow displaying elongated structures in the streamwise direction. The actual spacing between gridpoints is

$$h_1 = 2 \times 2^{-\frac{1}{3}} \frac{2\pi}{N}, \quad h_2 = 2^{-\frac{1}{3}} \frac{2\pi}{N}, \quad h_3 = 2^{-\frac{1}{3}} \frac{2\pi}{N}, \tag{85}$$

with $N = 128$. The characteristic scale corresponding to the index m is computed as

$$r_m = 2^m (h_1 h_2 h_3)^{\frac{1}{3}}, \tag{86}$$

and the wavenumber k_m is given by (68).

The three-dimensional dual spectra are computed as the trace of (72), and those for the shear flow are displayed in figure 11. Again, there is good agreement between the Fourier radial spectrum of the flow and the wavelet spectrum at large scales and again some small disagreement can be seen at the small scales, where the spectrum becomes steeper. Slightly increased relative variance of the energies is again found at the small scales in the dual spectrum. We also compute the largest local kinetic energy in the computational domain, which is displayed as the upper line in the dual spectrum of figure 11. This illustrates fairly well that local energies at a scale can differ greatly from their mean values.

Next we compute the flatness factors. For every velocity component i and scale m, we average over all locations $\mathbf{i}$ and over all 7 q-components (one could also define flatness factors for each q-component). The values of $F_i(k_m)$ are displayed in figure 12 for the case of isotropic turbulence. At the large scales (small k_m), the number of coefficients is very low, so that the statistics are poorly converged. However, it appears that the large scales tend to the Gaussian value $F = 3$. The flatness of the small scales increases quickly, and in the same fashion for all three velocity components, as expected for an isotropic flow. Figure 13 shows the corresponding results for the homogeneous shear flow. Again the large scales appear Gaussian, although the poor statistical sampling there precludes us from making any definite

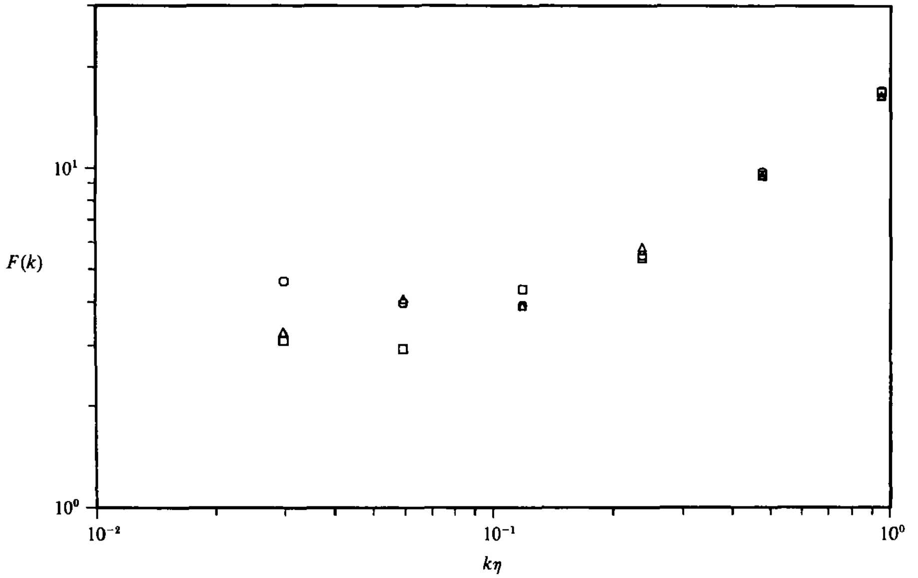

FIGURE 12. Flatness factors of the wavelet coefficients computed from the simulation of isotropic turbulence. Different symbols correspond to different velocity components: □, u; ○, v; △, w.

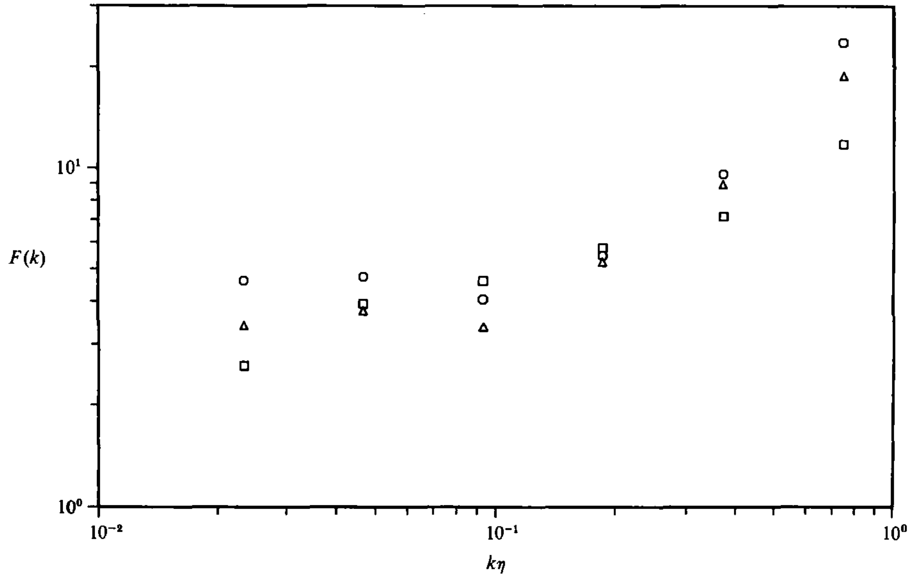

FIGURE 13. Flatness factors of the wavelet coefficients computed from the simulation of homogeneous sheared turbulence. Different symbols correspond to different velocity components: □, u; ○, v; △, w.

statements. The flatness of the small scales is quite different for each velocity component, indicative of small-scale anisotropy. The transverse velocity components (in the plane perpendicular to the streamwise direction) tend to be considerably more intermittent than the streamwise component for the two smallest scales. This seems consistent with the view that elongated small-scale vortical structures exist, aligned with the streamwise direction of the flow. On the other hand, the contribution to kinetic energy by the streamwise component is considerably higher than those of the transverse components (see Rogers & Moin 1986). The energy is dominated by the larger scales (here at $k\eta \approx 10^{-1}$), and we notice that at that scale the flatness of the streamwise component is now the largest. Thus the component dominating the total energy is also the most intermittent at that particular scale.

5. Energy transfer and flux in the wavelet representation

We now turn our attention to the energy transfer in the wavelet representation by analysing the results of direct numerical simulations in three dimensions.

5.1. *Dual spectra of transfer and flux*

By analogy to the relation between the local wavelet energies and the Fourier spectral energy density obtained in §4.1, we obtain

$$T(k_m) = \frac{2^{-2m}(h_1 h_2 h_3)^{\frac{1}{3}}}{2\pi \ln(2)} \langle t^{(m)}[i] \rangle, \tag{87}$$

where the average extends over all points $[i]$. The spatial variability of $t^m[i]$ is measured by its standard deviation in units of $T(k_m)$ as

$$\sigma_{(T)}(k_m) = \frac{2^{-2m}(h_1 h_2 h_3)^{\frac{1}{3}}}{2\pi \ln 2} (\langle t^{(m)}[i]^2 \rangle - \langle t^{(m)}[i] \rangle^2)^{\frac{1}{2}}, \tag{88}$$

where the average again extends over all points $[i]$. The relations that hold for the dual spectrum of the flux π are slightly different because it already corresponds to an integral of transfer over scales. To obtain the spectral value equivalent to (4), we average the flux over all locations $[i]$, and from an argument similar to the one leading to (72) (except that here we do not need to divide by Δk_m, because an integration or sum is already performed), one obtains

$$\pi(k_m) = 2^{-3m} \langle \pi^{(m)}[i] \rangle, \tag{89}$$

and the variability, in the units of $\pi(k_m)$, is then quantified as

$$\sigma_{(\pi)}(k_m) = 2^{-3m}(\langle \pi^{(m)}[i]^2 \rangle - \langle \pi^{(m)}[i] \rangle^2)^{\frac{1}{2}}. \tag{90}$$

5.2. *Calculation of dual transfer and flux spectra*

We compute the transfer $t^{(m)}[i]$ for both three-dimensional flow fields from direct numerical simulations. To compute the wavelet transform of the nonlinear terms of the Navier–Stokes equation, we need both the velocity and pressure fields, the latter is computed from the velocity using the Poisson equation

$$\frac{1}{\rho} \frac{\partial^2 p}{\partial x_j^2} = -\left(\frac{\partial u_i}{\partial x_j}\right)\left(\frac{\partial u_j}{\partial x_i}\right). \tag{91}$$

This is the ('slow') part of the pressure associated with the fluctuating part of the velocity field. We compute the wavelet transform of the velocity and the nonlinear terms and evaluate $t^{(m)}[i]$ according to its definition in (56), and then we evaluate the dual spectrum of the transfer.

Figure 14 shows the dual transfer spectrum $T(k_m)$ and $T(k_m) \pm \sigma_{(t)}^{(m)}$ in Kolmogorov units, computed from the homogeneous shear flow. The mean transfer (circles) is negative for low wavenumbers and positive at high wavenumbers. The solid line is the corresponding radial Fourier transfer spectrum and is in reasonable agreement

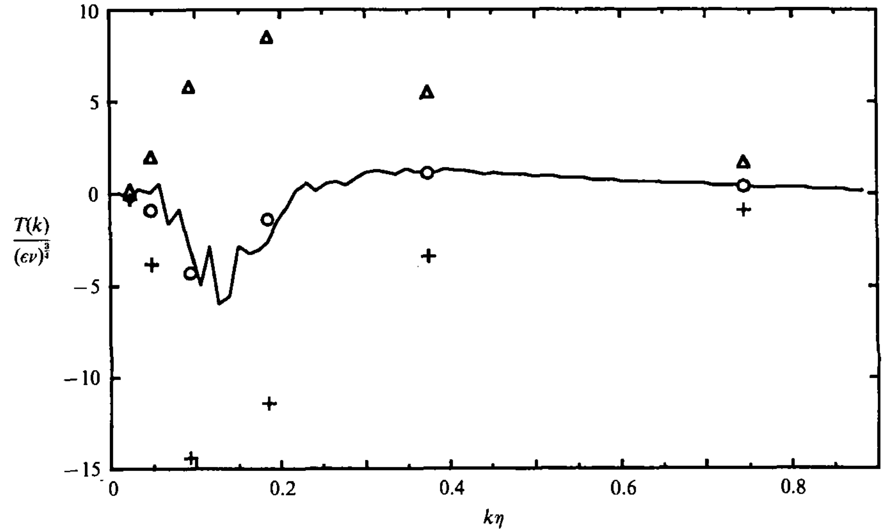

FIGURE 14. Dual spectrum of transfer of kinetic energy for homogeneous shear simulation, normalized by Kolmogorov units. ——, Usual Fourier transfer; ○, mean wavelet spectrum; △ and +, wavelet mean, plus and minus one standard deviation computed from the spatial fluctuations at every scale.

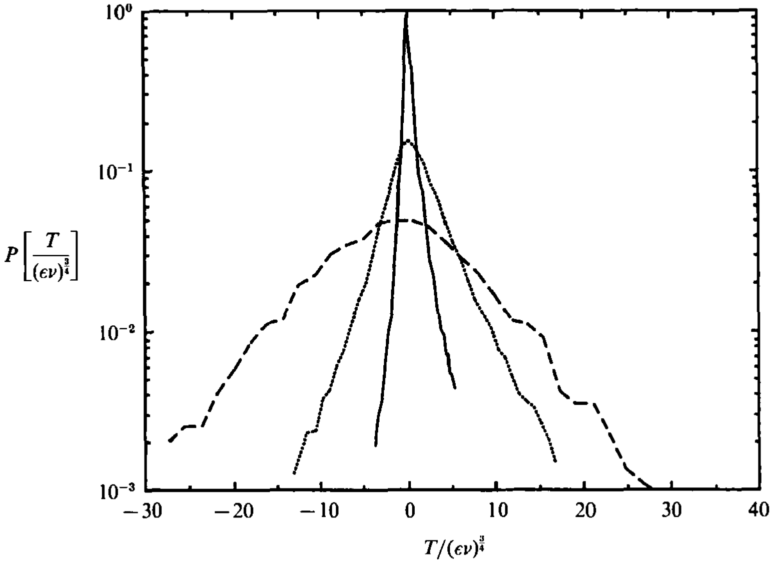

FIGURE 15. Probability density function of spatial fluctuations of local transfer for the homogeneous shear flow simulation, for scales corresponding to: ——, $m = 1$, $k\eta = 0.74$; ····, $m = 2$, $k\eta = 0.37$; ---, $m = 3$, $k\eta = 0.18$.

with the mean wavelet transfer. As expected, on average energy is being transferred from large to small scales. However, the standard deviation $\sigma_{(t)}^{(m)}$ is very large, implying that the transfer of energy is locally often quite far from its mean value. This is borne out more clearly in the probability-density of $t^{(m)}[\boldsymbol{i}]$ in figure 15, where large deviations from the mean are visible, for both positive and negative values. Note that the long tails of the distributions are of the exponential type, while the central portions of the distributions are more nearly Gaussian. Such distributions

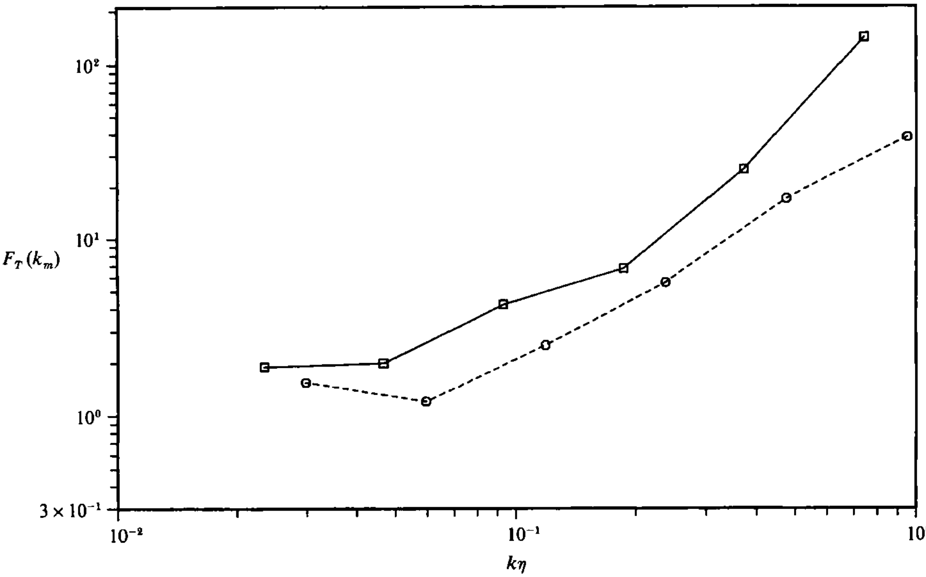

FIGURE 16. Flatness factor of the local transfer of kinetic energy at every scale $k_m\eta$. □, Homogeneous shear turbulence; ○, isotropic turbulence case.

have also been observed for velocity increments (Gagne 1989). (As m increases the number of samples $2^{3(7-m)}$ decreases and we cannot accurately measure the distribution functions for $m \geqslant 4$.) The same calculations for the isotropic flow yield similar results, the only difference being that the mean transfer $T(k_m)$ is considerably smaller in Kolmogorov units than in the shear flow. This is mainly due to the decaying nature of this flow, there being more energy dissipation than instantaneous nonlinear transfer, while in the shear flow at $St = 12$ the energy is growing. However, we again observe large spatial deviations from the spectral mean, and the p.d.f. of the energy transfer in the case of the isotropic field again displays non-Gaussian tails (II).

To quantify more precisely the deviations from Gaussian behaviour we compute $F_T(k_m)$, the flatness factor of the transfer, at every scale for both flows (figure 16). Again, the results at large scales are not accurate owing to insufficient samples, but it is clear that there is a fast increase of the flatness factor at small scales (away from the Gaussian value $F_T(k_m) = 3$). This increase is qualitatively very similar in both flows, but the shear flow has slightly higher flatness which may be due to the higher Reynolds number of the shear flow.

We next compute the flux of kinetic energy at every scale of motion according to (59). The Fourier spectrum of the flux is computed from the transfer according to (4). The dual spectrum of flux thus obtained is shown in figure 17 for the homogeneous shear turbulence case. On the average, there is a flux of energy from large to small scales, but large spatial fluctuations of $\pi^{(m)}[i]$ are visible in the dual spectrum. The agreement between the mean wavelet and Fourier spectra is not very good; this is due to the width of the wavelet transform in Fourier space, which causes slight differences in the transfer, these then accumulate when computing the flux. The only constraint given by the exact reconstruction properties of the orthonormal wavelets is that the total flux at the smallest scale must equal the overall sum of the transfer, which is zero. The dual spectrum of the flux for the isotropic turbulent flow is quite similar. To quantify the fluctuations in more detail, we again show probability density functions of the flux at different scales. Figure 18 shows the p.d.f. for the

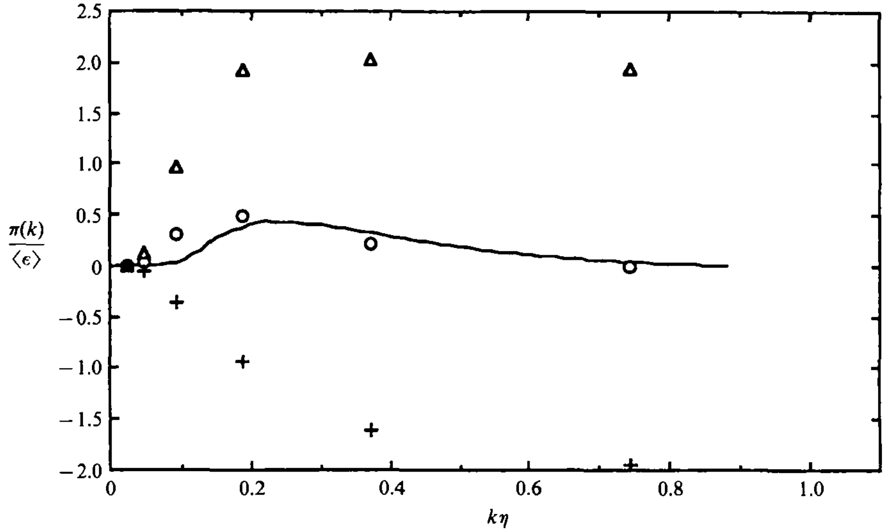

FIGURE 17. Dual spectrum of the flux of kinetic energy from the homogeneous shear flow simulation, in Kolmogorov units. ——, Fourier flux; ○, mean wavelet spectrum; △ and +, wavelet mean, plus and minus one standard deviation computed from the spatial fluctuations at every scale.

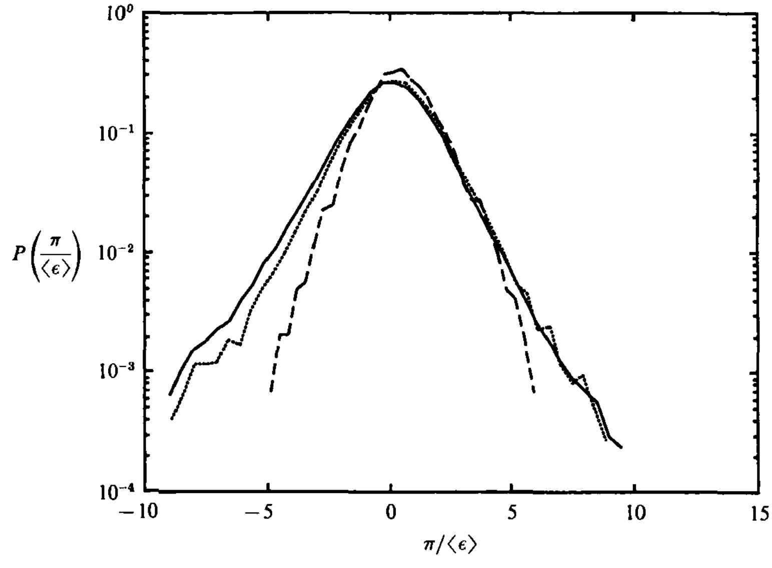

FIGURE 18. Probability density function of spatial fluctuations of local flux of kinetic energy for the homogeneous shear simulation, for scales corresponding to: ——, $m = 1$, $k\eta = 0.74$; ····, $m = 2$, $k\eta = 0.37$; ---, $m = 3$, $k\eta = 0.18$.

homogeneous shear-flow simulation. These clearly show that while the spatial average of π is positive, there are many instances where $\pi < 0$ (we do not call such events 'backscatter', because this terminology usually refers to the flux to, or from, smaller scales only, and not to $\pi^{(m)}[i]$, which also includes spatial flux due to sweeping). The tails of the distributions again show clear deviations from Gaussianity: they are of the exponential type for both positive and negative values.

Returning to the local values of flux, we stress that $\pi^{(m)}[i]$ does not only represent flux of energy between different scales, but also flux from one location to another, at the same scale (spatial mixing of energy, see Kraichnan 1974). The question of flux only to or from smaller scales, requires a more detailed decomposition of the nonlinear terms, which will be addressed in §6.

5.3. *Influence of wavelet function on energy and transfer statistics*

For the statistical analysis to be complete, one needs to ascertain how robust the results of the preceding sections are with respect to the precise wavelet used. Here we discuss several possible choices of orthonormal wavelets. We have already mentioned the LMB wavelets, with exponential decay in x-space and k^{-4} decay in Fourier space, that were used in the preceding sections. A very simple choice of orthonormal 'wavelet' is the Haar base, corresponding to sharp pulses in physical space, but poor localization in spectral space. This is the wavelet analogy of a french top-hat filter. At the other extreme of the uncertainty principle for 'wave-packets' or band-pass filters, we have sharp filters in Fourier space, with very poor spatial localization. The precise form that allows it to be put into the form of a wavelet will here be called a 'Fourierlet' (more details can be found in Appendix B of II). Another very interesting family of wavelets, constructed by Daubechies (1988) has compact support in physical space and increasing smoothness as the support increases. We plot the discrete version $g[k]$ of these different wavelets in figure 19 (*a–d*). More details on the precise form of such wavelets are given in Appendix B of II. In the rest of this section we explore the sensitivity of the results presented in the preceding section with respect to the precise wavelet function used.

For that purpose we compute the dual spectra of transfer using all the above wavelets, and we also compute the p.d.f.s of the transfer for these wavelets. To simplify the numerical implementation (and to be able to use the same numerical code), we compute all convolutions in Fourier space for all wavelets. It is important to point out that such a procedure is not optimal for bases with support smaller than $\log_2(N)$ (where N is the number of grid-points), such as the Haar base. There the convolutions would be more efficiently performed in physical space (with $O(N)$ rather than $O(N\log[N])$ operations).

The results for the different wavelets are displayed in figure 20 (*a*), showing the probability densities of the transfer at $m = 3$. As one would expect, the spatial variability increases slightly with better localization in physical space, but the main features, such as large deviations from the mean of $t^{(m)}[i]$, exponential tails, etc. are quite similar in each case. For completeness, we also compare the statistics of the local kinetic energies for different wavelets. The results are shown in figure 20 (*b*), where the local energies are normalized in the same fashion as in the dual spectrum of figure 11. Again there is good agreement between different wavelets at this level of description. We conclude that from a statistical point of view, it does not matter very much what system of orthonormal wavelet basis functions is used. The observation that the results using 'Fourierlets' do not deviate greatly from the others has important implications for interpreting studies using Fourier band-pass filtered fields, such as recent work by Domaradski & Rogallo (1990). Nevertheless, it must be pointed out that the 'Fourierlets' do not comply with discrete orthonormality. This is due to the finite domain truncation (or assumption of periodicity) of the convolutions. While this is no problem for the other wavelets that decay very quickly in space (even the LMB wavelets are essentially zero at the boundaries), the x^{-1} decay of the Fourierlet basis functions means that it is non-zero

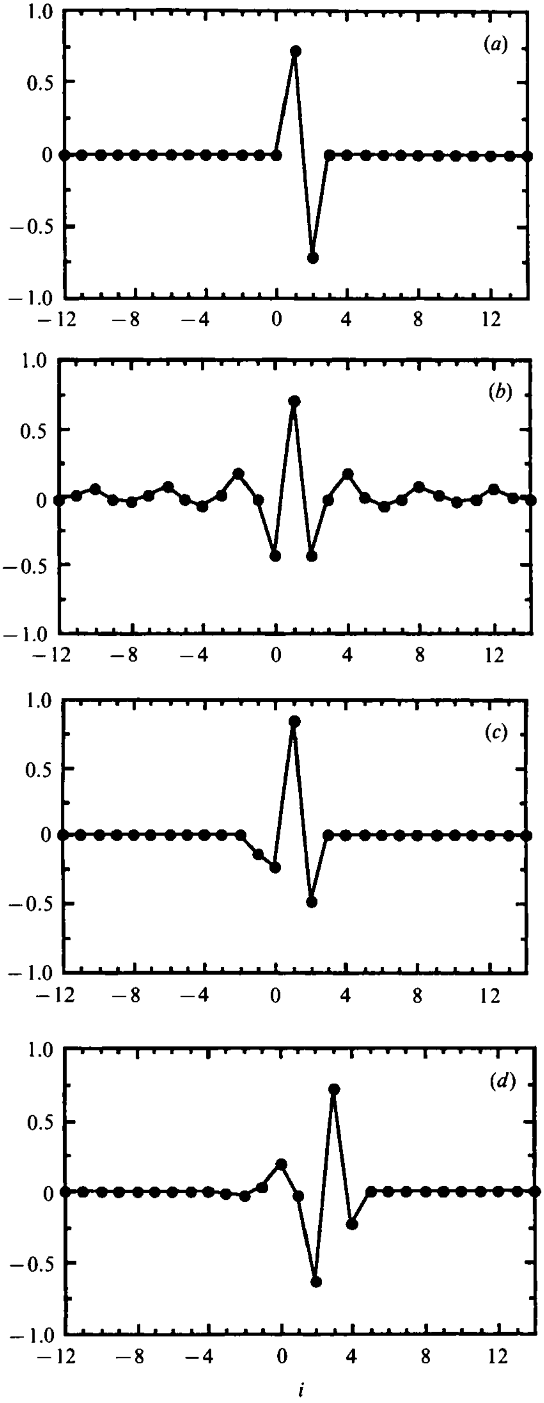

FIGURE 19. Examples of discrete wavelets: the filter $g[k]$. (*a*) Corresponds to the Haar basis; (*b*) 'Fourierlet' consisting of sharp filtering in Fourier space; (*c*) Daubechies wavelet of compact support on 4 grid-points; (*d*) Daubechies wavelet of compact support on 8 grid-points. The convention for the index used here is that $i = 1$ represents $x = 0$.

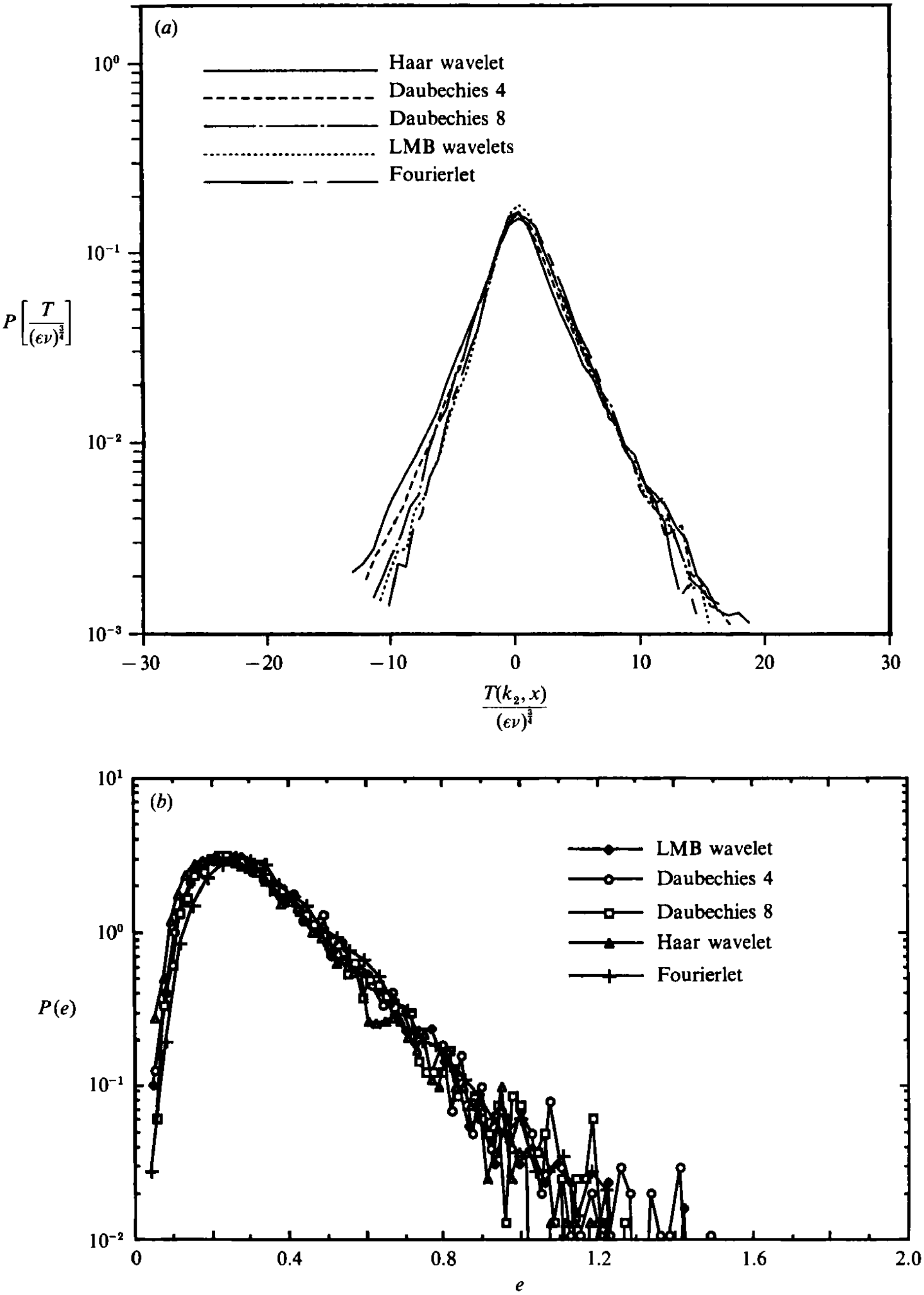

FIGURE 20. (*a*) Probability density distribution of transfer of kinetic energy at scale $m = 3$ computed using different wavelet basis functions. (*b*) Probability density distribution of the local kinetic energy.

at the boundaries, causing considerable inaccuracies (even for periodic data because the wavelet itself is truncated).

Finally, we remark that the wavelets used here all share an important property, namely octave discretization of scales. One may expect different results if one used continuous wavelets, or discretization of scales on a markedly different grid.

6. Detailed nonlinear interactions in wavelet space

In the preceding section we studied the net transfer to, and flux through a certain scale and location, without discriminating the scales between which such energy transfer is occurring. The analysis was relatively straightforward, as we only had to wavelet transform the velocity field and the nonlinear terms and compute the appropriate contractions. It is apparent in the continuously wavelet-transformed Navier–Stokes equation (44) that the formulation quickly becomes intractable when considering in detail all interactions between triads of scales and locations. This situation does not improve when using the orthonormal wavelet basis functions, for which the Navier–Stokes equations take on the form

$$\frac{\partial}{\partial t} w_i^{(m,q)}[\boldsymbol{i}] = -\sum_{m'}\sum_{m''}\sum_{\boldsymbol{j}'}\sum_{\boldsymbol{j}''}\sum_{q'}\sum_{q''} w_i^{(m',q')}[\boldsymbol{j}']\, w_j^{(m'',q'')}[\boldsymbol{j}'']\, I_{j(q,q',q'')}^{(m,m',m'')}[\boldsymbol{i},\boldsymbol{j}',\boldsymbol{j}''] - \dots, \tag{92}$$

where

$$I_{j(q,q',q'')}^{(m,m',m'')}[\boldsymbol{i},\boldsymbol{j}',\boldsymbol{j}''] = \iiint \Psi^{(m,q)}(\boldsymbol{x}-2^m\boldsymbol{i}) \frac{\partial}{\partial x_j}[\Psi^{(m',q')}(\boldsymbol{x}-2^{m'}\boldsymbol{j}')\, \Psi^{(m'',q'')}(\boldsymbol{x}-2^{m''}\boldsymbol{j}'')]\, \mathrm{d}^3\boldsymbol{x}; \tag{93}$$

and in addition there are pressure and viscous terms, etc. There are interactions among triads of scales and locations, as well as among the internal degrees of freedom (q, q'', q''). We will not dwell on the subject, but we point out that some meaningful approximations to $I_{j(q,q',q'')}^{(m,m',m'')}[\boldsymbol{i},\boldsymbol{j}',\boldsymbol{j}'']$ can be made in view of the localization properties of $\Psi^{(m,q)}(\boldsymbol{x}-2^m\boldsymbol{j}')$. Such a study was made recently by Nakano (1988), who then extends the method of Direct Interaction Approximation to such a formulation (see also Siggia 1977). It is important to notice however that the basis functions used here are fixed in an Eulerian frame of reference: this means that there can be strong interactions between modes at the same location corresponding to distant scales of motion because of the sweeping of small scales by large ones. To eliminate this problem, one needs to consider basis functions advected by the larger scales (this has been proposed in an interesting paper by Zimin 1981), but this is outside the scope of the present effort.

In order to study the transfer involving scales of motion that are smaller than r_m (this has relevance for large-eddy simulations, Rogallo & Moin 1984), we start by performing the sums of (92) over all $q', q'', \boldsymbol{j}', \boldsymbol{j}''$ and over all scales (m', m'') but excluding the terms where both $m' \geqslant m$ and $m'' \geqslant m$. In practice, this is done as follows: we recall that the velocity field can be computed from the wavelet coefficients according to

$$u_i(\boldsymbol{x}) = \sum_{m=1}^{M} u_i^{(m)}(\boldsymbol{x}), \tag{94}$$

where
$$u_i^{(m)}(\boldsymbol{x}) = \sum_{\boldsymbol{i}} \sum_{q=1}^{7} w_i^{(m,q)}[\boldsymbol{i}]\, \Psi^{(m,q)}(\boldsymbol{x}-2^m\boldsymbol{i}), \tag{95}$$

is a band-pass filtered version of the field. Let us now decompose the velocity field according to large- and small-scale contributions,

$$u_i(\boldsymbol{x}) = u_i^{<m}(\boldsymbol{x}) + u_i^{>m}(\boldsymbol{x}) = \sum_{n=1}^{m-1} [u_i^{(n)}(\boldsymbol{x})] + \sum_{n=m}^{M} [u_i^{(n)}(\boldsymbol{x})]. \tag{96}$$

This amounts to low- and high-pass filtered fields, using the wavelet transform. Now we decompose the nonlinear advection terms as

$$\frac{\partial}{\partial x_j}(u_i u_j) = \frac{\partial}{\partial x_j}[u_i u_j - u_i^{>m} u_j^{>m}] + \frac{\partial}{\partial x_j}(u_i^{>m} u_j^{>m}). \tag{97}$$

The first term on the right-hand side represents all possible velocity interactions with the scales smaller than m, this being the term in which we are interested. For the pressure $p(\boldsymbol{x})$, we consider the same decomposition as (96),

$$p(\boldsymbol{x}) = p^{<m}(\boldsymbol{x}) + p^{>m}(\boldsymbol{x}) = \sum_{n=1}^{m-1} [p^{(n)}(\boldsymbol{x})] + \sum_{n=m}^{M} [p^{(n)}(\boldsymbol{x})], \tag{98}$$

where $p^{(n)}(\boldsymbol{x})$ is obtained as in (95) from the wavelet coefficients of the pressure field. We are interested in the small-scale pressure field $p^{<m}(\boldsymbol{x})$, which could also be computed from the Poisson equation involving $\partial_i \partial_j [u_i u_j - (u_i u_j)^{>m}]$ on the right-hand side. Notice that this decomposition of pressure has a different form to the decomposition of the advection terms in (97). The decomposition used here is the one in which the 'large-scale' pressure field $p^{>m}(\boldsymbol{x})$ would be consistent with a divergence-free 'large-scale' velocity field $u_i^{>m}(\boldsymbol{x})$.

Next we take the wavelet transform of these terms and form the following expression:

$$t^{(m,n)}[\boldsymbol{i}] = \sum_{i=1}^{3} \sum_{q=1}^{7} w_i^{(m,q)}[\boldsymbol{i}] \left\{ \frac{\partial}{\partial x_j}[u_i u_j - u_i^{>n} u_j^{>n}] + \rho^{-1} \frac{\partial}{\partial x_i} p^{<n} \right\}^{(m,q)} [\boldsymbol{i}]. \tag{99}$$

This is the transfer of energy between scales m and all scales smaller than n, a quantity that is analogous to the Fourier transfer spectrum $T(k \mid k_n)$, defined as the total contribution to $T(k)$ from triads of wavenumbers $(k, q, k-q)$ having $k < k_n$ and at least one of the other two legs larger than k_n (see e.g. Kraichnan 1976). Needless to say, there are many other decompositions that could be performed, e.g. one could consider the transfer between bands of scales m and n only, or the transfer between bands m, n and positions separated by some distance, etc. More detailed studies in that spirit should be attempted in the future. It has been shown by Domaradski & Rogallo (1990), for example, that interesting conclusions can be reached from the analysis of entire triads of interactions, rather than the contracted form of $T(k \mid k_n)$; we will return to this point later. Here we concentrate on the problem of transfer to smaller scales.

6.1. *Dual bispectrum of transfer*

In this section we compute $t^{(m,n)}[\boldsymbol{i}]$ from the numerical simulations. The filtered fields $u_i^{>m}(\boldsymbol{x})$ and $p^{<m}(\boldsymbol{x})$ are computed using the wavelet coefficients of the velocity field and pressure field, and $t^{(m,n)}[\boldsymbol{i}]$ is obtained from its definition (99), for all $m > n$. Let us fix the index n at some value and compute the mean spatial value of $t^{(m,n)}[\boldsymbol{i}]$ as well as its variance at every scale. This allows the construction of a 'dual spectrum' of the 'subgrid' transfer by plotting the mean $T(k_m \mid k_n)$, and $T(k_m \mid k_n) \pm \sigma_{m \mid n}$, where $\sigma_{m \mid n}$ is the root-mean-square of the spatial fluctuations of the transfer. The expressions used are exactly the same as (87) and (88), replacing $t^{(m)}[\boldsymbol{i}]$ with $t^{(m,n)}[\boldsymbol{i}]$. Such a representation as a function of all the m and n will be called the dual bispectrum of transfer to smaller scales.

In figure 21(*a–c*) we show this spectrum for $n = 1$, $n = 2$ and $n = 3$, for the

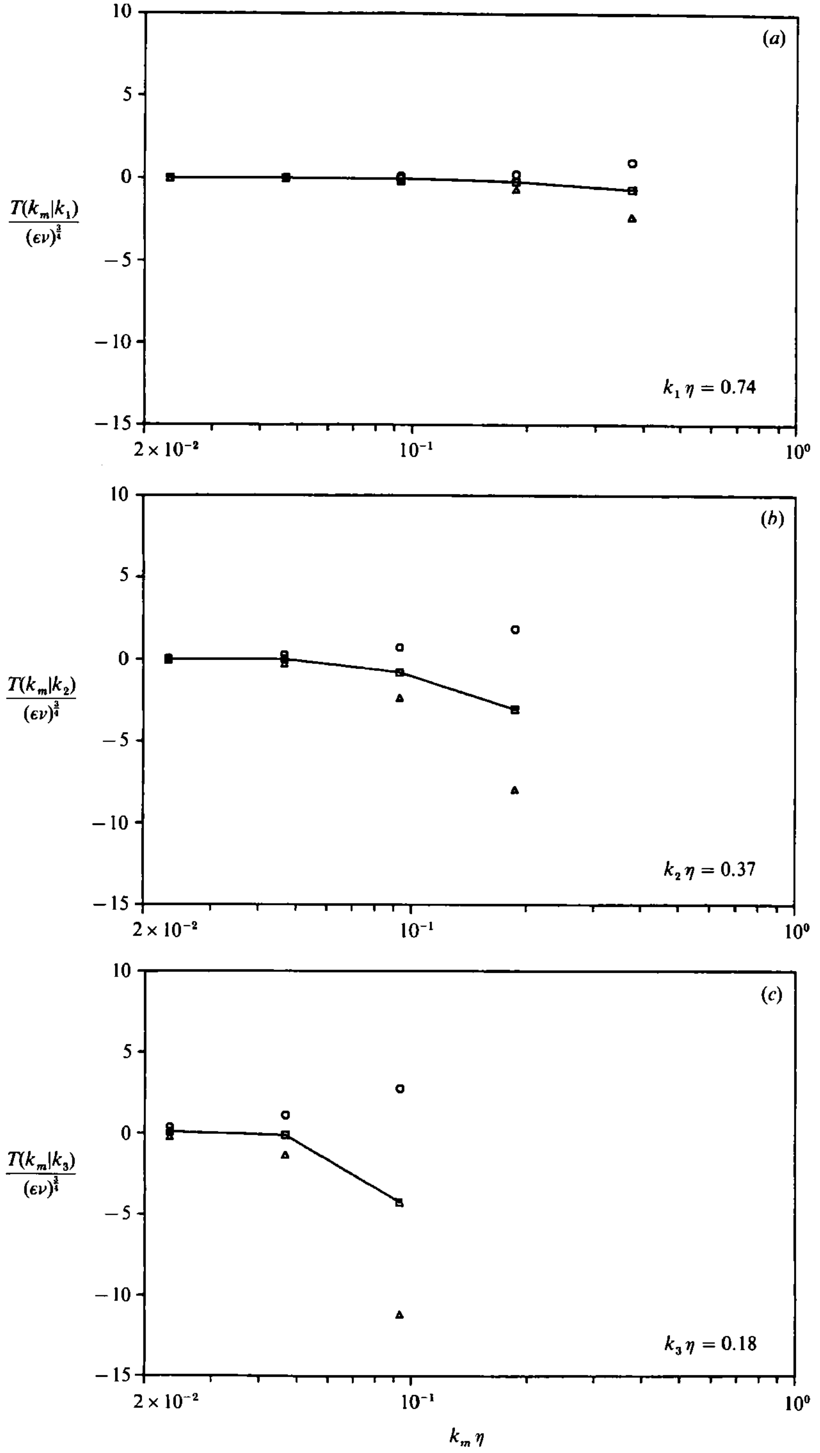

FIGURE 21. (*a–c*) Dual bi-spectra of transfer of kinetic energy for the homogeneous shear simulation. Squares correspond to the spatial mean value $t^{(m,n)}[i]$, analogous to the transfer $T(k,k')$ in Fourier analysis. ○ and △, mean, plus and minus one standard deviation computed from the spatial variability of $t^{(m,n)}[i]$. (*a*) is for the transfer from $k = k_m$ to $k' = k_n$ for $n = 1$; (*b*) for $n = 2$ and (*c*) for $n = 3$.

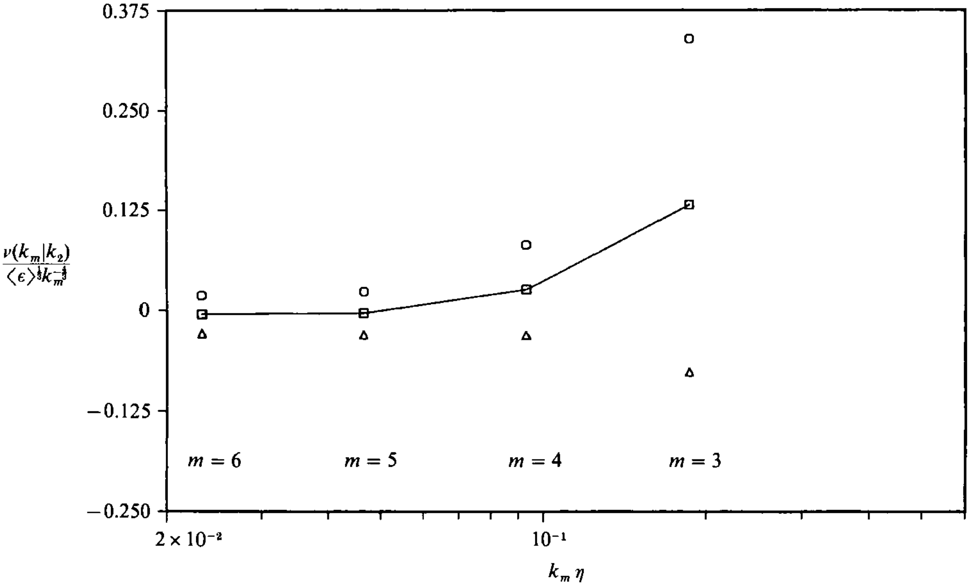

FIGURE 22. Dual spectrum of effective eddy viscosity felt by scales k_m due to all scales smaller than k_n, with $n = 2$. □, Spatial mean value, analogous to the spectral effective eddy viscosity $\nu(k\,|\,k')$ in Fourier analysis. ○ and △, mean, plus and minus one standard deviation computed from its spatial variability.

homogeneous shear calculation. The isotropic flow shows very similar behaviour. It can be seen that the majority of the transfer occurs at $m = n+1$, meaning that the transfer to smaller scales is local in scale. This is the same conclusion reached in several other studies, see e.g. Domaradski & Rogallo (1990) (nevertheless, these authors showed that the third scale involved in the transfer is about an order of magnitude larger implying non-local triad interactions). Here we show not only that the transfer is local in scale, but also that it fluctuates in space, with the largest variability occurring at the smallest scale $n+1$. Another vital observation is that of detailed backscatter. For all n, there are many instances where the transfer is positive, meaning that larger scales are gaining energy from the small ones instead of the other way around.

The analysis can be made more clear by defining an effective eddy viscosity

$$\nu^{(m,\,n)}[\mathbf{i}] = -\frac{t^{(m,\,n)}[\mathbf{i}]}{2k_m^2\, e^{(m)}[\mathbf{i}]}, \tag{100}$$

where $e^{(m)}[\mathbf{i}]$ is the local kinetic energy that has been analysed in §4. We define again a dual spectrum of this quantity by considering its mean value and variance at every scale. We focus on some value of n, say $n = 2$. That is, we consider the eddy viscosity acting on scales of size m, owing to scales smaller or equal to n (or with wavenumbers smaller than $k_2\,\eta = 0.37$ in the case of the homogeneous shear flow). For purposes of normalizing the eddy viscosity, we do not use viscous scales, but rather 'inertial range' ones. In figure 22 we show the dual spectrum of effective eddy viscosity computed for the homogeneous shear flow, with $n = 2$. There is a 'cusp' near the cutoff scale, caused by the prevalent transfer of energy from neighbouring scales and the value slightly negative at the largest scales indicating a (weak) inverse cascade

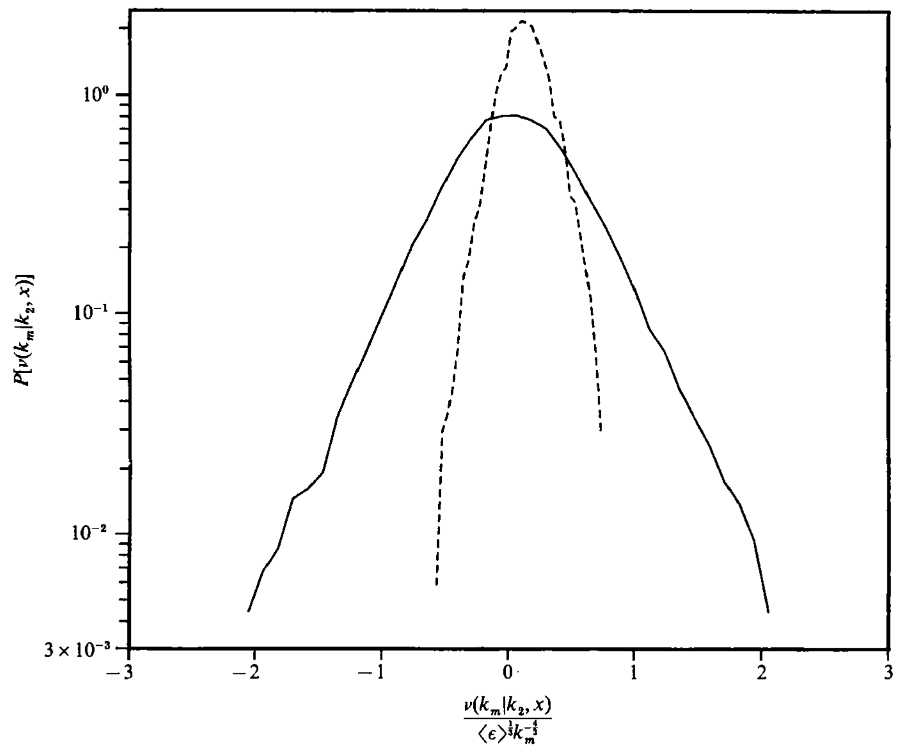

FIGURE 23. Probability density functions of the spatial distribution of effective eddy viscosity felt by scales k_m due to all scales smaller than k_n, with $n = 2$. ——, $m = 3$, $k\eta = 0.18$; ---, $m = k\eta = 0.09$.

of energy from very small scales to largest ones. This behaviour was also observed in Domaradski & Rogallo (1990) for the case of isotropic turbulence. The main point to be made here, however, is that this representation clearly shows that negative local eddy viscosities are present at all scales. The spatial fluctuations of this quantity become more pronounced as one approaches the cutoff limit $m = n$. To quantify this better, we consider the probability density function of $\nu^{(m,\,n-2)}[\mathbf{i}]$, plotted in figure 23 in the same units as the dual spectrum. At the smallest scale near the cutoff ($m = 3$) we observe long tails, again of the exponential type. There is a significant fraction of space (close to 50%), where $\nu^{(m,\,n-2)}[\mathbf{i}] = \nu(k_m, k_2, \mathbf{x})$ is negative.

6.2. *Spatial statistics of energy flux to smaller scales*

In large-eddy simulations, a quantity of great importance is the effective sink of kinetic energy due to the unresolved scales of motion (Rogallo & Moin 1984). This is needed in addition to the molecular dissipation to damp the equations sufficiently. In the Fourier representation, this sink of energy is given as a flux

$$\pi_{\mathrm{sg}}(k_{\mathrm{c}}) = -\int_{k=0}^{k_{\mathrm{c}}} T(k\,|\,k_{\mathrm{c}})\,\mathrm{d}k, \qquad (101)$$

where $T(k\,|\,k_{\mathrm{c}})$ is the transfer of energy from scales $k < k_{\mathrm{c}}$ involving triads with wavenumbers larger than k_{c} defined in the previous section.

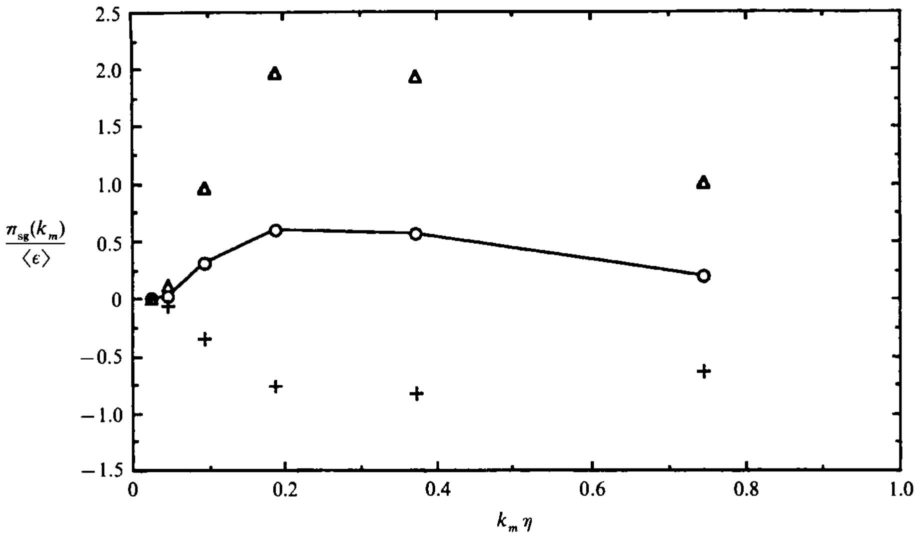

FIGURE 24. Dual spectrum of the flux of kinetic energy from interactions with all smaller scales of motion (flux to or from the subgrid scales), for the homogeneous shear flow simulation. ○, Mean wavelet spectrum; △ and ×, wavelet mean, plus and minus one standard deviation computed from the spatial fluctuations at every scale.

The analogous definition in the wavelet representation is the local 'subgrid' flux of energy to smaller scales,

$$\pi_{sg}^{(m)}[\boldsymbol{i}] = -\sum_{k=m}^{M} 2^{3(M-k)} t^{(k,m)}[2^{m-k}\boldsymbol{i}]. \tag{102}$$

This differs from the quantity considered in §5 because it represents the flux of energy at some location, caused only by interactions with scales smaller than m. Loosely speaking, if we consider that taking the wavelet transform and then adding over all scales larger than m is similar to low-pass filtering the fields as is usually done for large eddy simulations, then $\pi_{sg}^{(m)}[\boldsymbol{i}]$ is analogous to (Leonard 1974)

$$\epsilon_{sg}(\boldsymbol{x}) = (\overline{u_i}\frac{\partial}{\partial x_j}(\overline{u_i u_j} - \overline{\overline{u}_i\,\overline{u}_j}), \tag{103}$$

where an overbar means the filtering operation. We point out that $\pi_{sg}^{(m)}[\boldsymbol{i}]$ also includes energy flux due to smaller scales that is really a spatial transport that would vanish after summing over all space (for homogeneous flows). This can be seen from (103) by exhibiting its divergence part

$$\epsilon_{sg}(\boldsymbol{x}) = \frac{\partial}{\partial x_j}[\overline{u_i}(\overline{u_i u_j} - \overline{\overline{u}_i\,\overline{u}_j})] - \overline{s_{ij}}(\overline{u_i u_j} - \overline{\overline{u}_i\,\overline{u}_j}). \tag{104}$$

Such a separation is not easily done with orthonormal wavelets (there is no simple relation between a wavelet and its derivatives), and so we restrict our attention to the combined terms given by (102).

The subgrid-scale flux $\pi_{sg}^{(m)}[\boldsymbol{i}]$ is computed in both the homogeneous shear flow and in the isotropic turbulence case. For both flows we again construct the dual spectrum, and obtain the probability density of the subgrid flux at every scale.

In figure 24 we show the dual spectrum computed from the homogeneous shear flow simulation, while figure 25 shows the probability distributions for the three

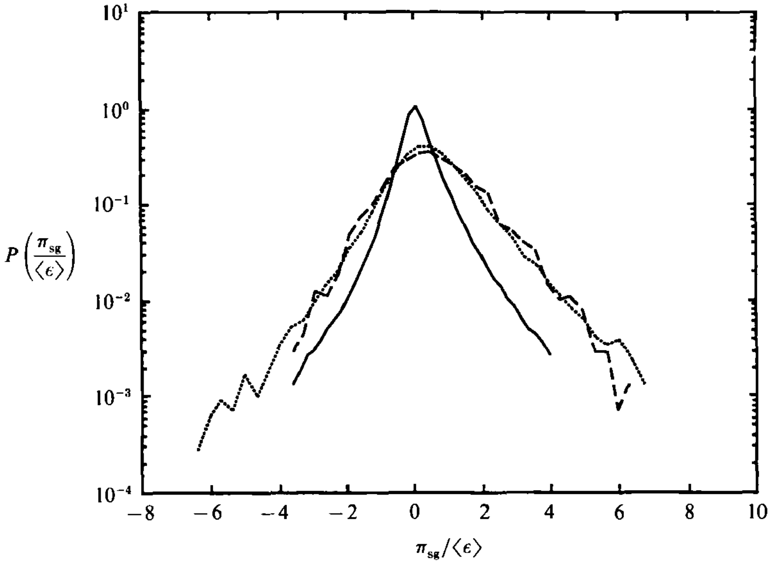

FIGURE 25. Probability density function of spatial fluctuations of local subgrid flux of kinetic energy for the homogeneous shear simulation, for scales corresponding to: ——, $m = 1$, $k\eta = 0.78$; ····, $m = 2$, $k\eta = 0.37$; – – –, $m = 3$, $k\eta = 0.18$.

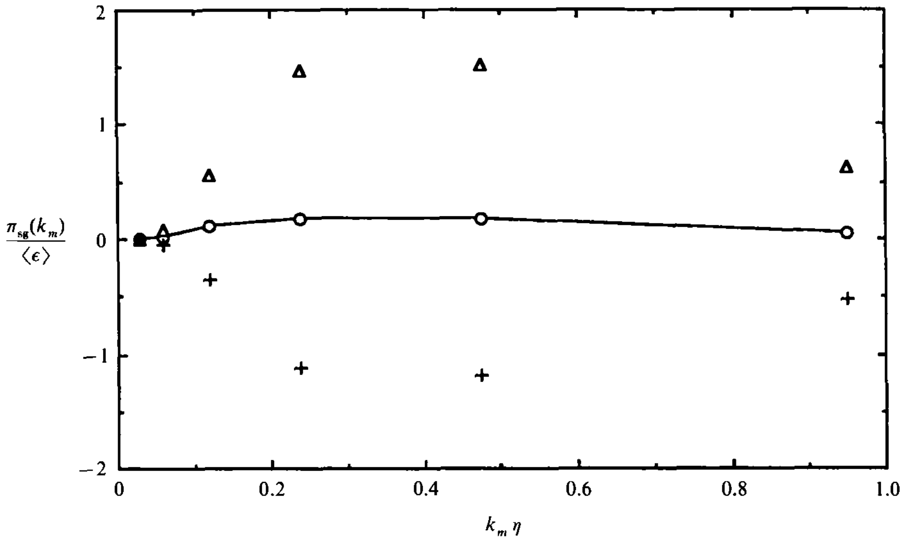

FIGURE 26. Dual spectrum of the flux of kinetic energy from interactions with all smaller scales of motion (flux to or from the subgrid scales), for the isotropic turbulence simulation. ○, Mean wavelet spectrum; △ and +, wavelet mean, plus and minus one standard deviation computed from the spatial fluctuations at every scale.

smallest scales. Figures 26 and 27 show the calculations for the isotropic turbulence case. We make the following observations: the mean subgrid flux is always positive, indicating that on the average, the subgrid scales extract energy from the large scales. There are strong spatial fluctuations, even though they are less pronounced for this subgrid flux π_{sg} than they were for the overall flux considered in §5. This is

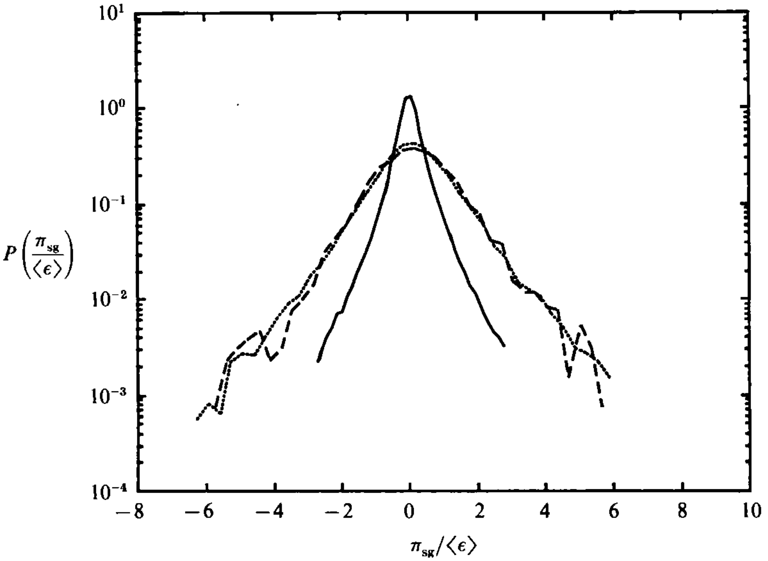

FIGURE 27. Probability density function of spatial fluctuations of local subgrid flux of kinetic energy for the isotropic turbulence simulation, for scales corresponding to: ——, $m = 1$, $k\eta = 0.94$; ····, $m = 2$, $k\eta = 0.47$; ----, $m = 3$, $k\eta = 0.23$.

because the latter also included flux due to sweeping by larger scales. The statistics of π_{sg} are far from Gaussian, exhibiting again very clearly long and exponential tails that indicate that the flux is very intermittent in space, at every scale of motion. Only the central portion of the distributions appears Gaussian. The subgrid flux is often negative, a phenomenon called local backscatter. The tails of the distributions are close to being symmetric and the positive average results from a delicate balance between large positive and moderate negative excursions. The phenomenon of local backscatter has also been observed recently during analysis of channel flow and compressible turbulence simulations (Piomelli *et al.* 1991), with very similar results concerning the fraction of points at which backscatter is observed.

The concept of backscatter (or eddy noise) was analysed from the spectral point of view by Rose (1977) and Leslie & Quarini (1979). There a spectral backscatter $U(k)$ is defined as the (negative) term that arises in spectral calculations (using the eddy-damped-quasi-normal-Markovian approximation) and that cannot be written in a form consistent with eddy-viscosity. It is therefore a 'spectral' backscatter term, and is in some sense an average over all space not explicitly related to the negative fluxes in physical space (for which one would also need phase information besides spectra). Thus a comparison with present results is unfortunately not possible. A recent stochastic backscatter model by Leith (1990) addresses (and implements) negative fluxes in physical space, and we shall return to this point in the next section.

Thus we have studied some dynamically relevant quantities associated with the nonlinear character of turbulence in two low-Reynolds number flows. This detailed analysis of the nonlinear terms was not facilitated by the use of wavelets, because of their rather complicated behaviour under differentiation, multiplication, etc. but the results of the analysis complement those of §§4 and 5.

7. Mixed cascade model

In this section we turn our attention to modelling some features of the observed quantities. In practice, the most useful quantities to model are the subgrid stresses that appear in the evolution equations for the resolved scales. These must then be modelled using the resolved quantities. On a scalar level, one is also interested in expressions for the drain of energy due to unresolved scales, as a function of the resolved ones. In this section we shall be even less ambitious and examine the general circumstances under which one could obtain intermittent fields containing both positive and negative values, as a phenomenological model for the local flux of energy to (or from) the small scales of motion.

It is safe to say that it has proved virtually impossible to understand and model small-scale intermittency in quantitative terms by making use of the Navier–Stokes equations (see e.g. Nelkin 1989). On the other hand, a variety of phenomenological cascade models which mimic intermittency have evolved (for a review of these models, see I). Most of them are concerned with models for positive definite quantities such as dissipation, and envisage a flux of kinetic energy to smaller scales which is positive everywhere and which can become very intermittent at small scales or at increasing Reynolds number. The well-known β model (Frisch, Sulem & Nelkin 1978) for example is a dynamically explicit model in terms of the local flux to smaller scales which is always either positive or zero. On the other hand, our analysis via wavelets has shown that the flux of kinetic energy is intermittent in space but is negative quite often. Such a behaviour is not included in previous phenomenological models, and these cannot be expected to model adequately the flux $\pi_{\mathrm{sg}}^{(m)}(\boldsymbol{x})$. In this chapter, we propose a simple extension to these models that incorporates the possibility that $\pi_{\mathrm{sg}}^{(m)}(\boldsymbol{x}) < 0$ locally.

Let us first review the basic physical and statistical ingredients of traditional cascade models in the inertial range. Physically, one expects portions of the fluid to stretch and fold, creating smaller scales of motion. This is modelled conceptually as a fragmentation process in which a fraction ξ of the energy flux is passed from a structure of size r to a smaller one of size $r' < r$ (ξ is a random variable that was denoted as M in I; here we use ξ in order to avoid confusion with the limit M of the scale index m). A common choice for the scale-ratio that is consistent with local transfer of energy is $r' = \frac{1}{2}r$. This means that in d dimensions each scale transfers energy to 2^d smaller ones. For global conservation of the flux at every stage of such a cascade, the random fraction ξ must have a mean value of 2^{-d}. Let $r = 2^{m+1}$ and $r' = 2^m$, and let $\Pi^{(m)}(B)$ be the flux associated with an 'eddy' at location B, of size 2^m arising from one of size $r = 2^{m+1}$ at location A. At every stage one writes

$$\Pi^{(m)}(B) = \xi \Pi^{(m+1)}(A). \tag{105}$$

Here $\Pi^{(m)}$ is the total flux of energy in a volume or eddy of size r_m; it is related to $\pi^{(m)}$, the flux per unit volume considered before in this paper, according to

$$\Pi^{(m)}(B) = r_m^d \, \pi^{(m)}(B). \tag{106}$$

At every location X, the flux is then given by a cumulative product of random terms, times the overall total flux (which is given by the mean dissipation and the volume of the large-scales $L^d = (2^M)^d$):

$$\Pi^{(m)}(X) = \xi \times \xi \times \ldots \times \xi \langle \epsilon \rangle L^3. \tag{107}$$

There are approximately $\log_2(L/r_m) \approx M - m$ such multipliers, which induces intermittent behaviour that increases with decreasing scale r. The hypothesis of scale

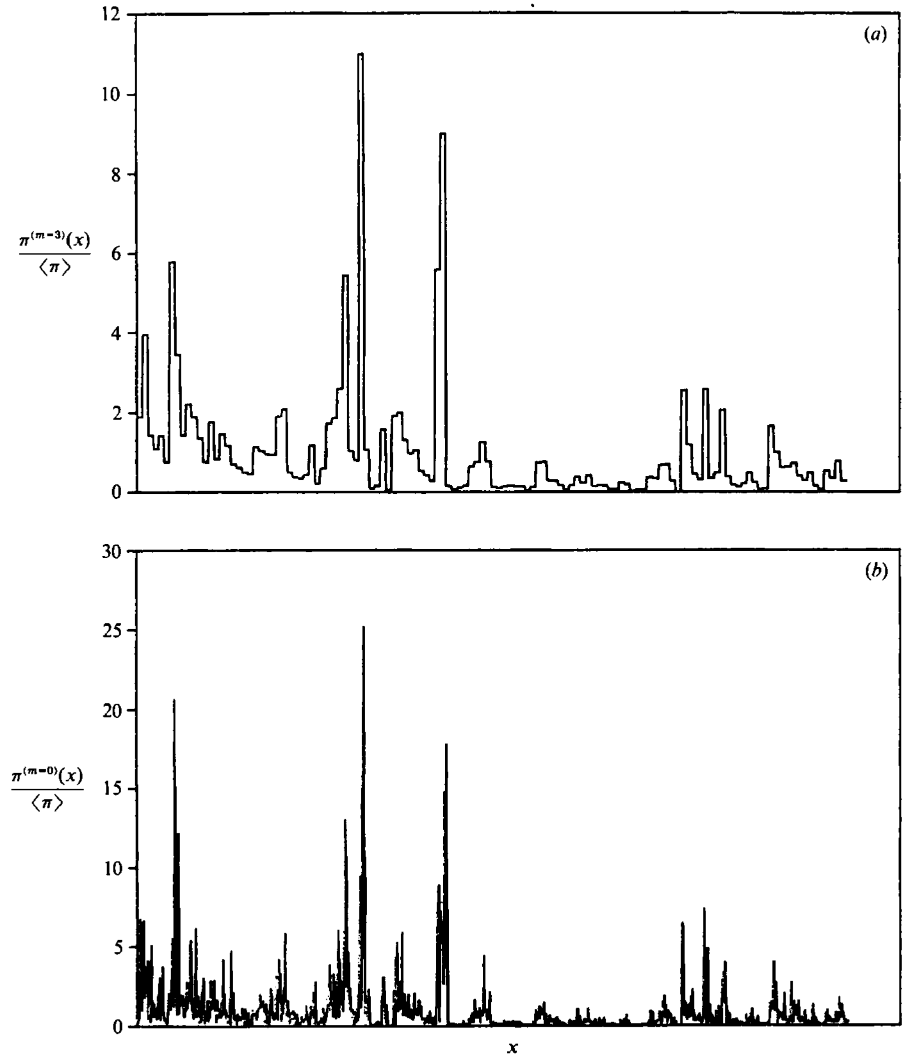

FIGURE 28. Illustration of an intermittent (multifractal) field generated by a multiplicative process in one dimension. The horizontal axis is successively divided into smaller halves, and the area under the curve is multiplied by a random multiplier ξ. The distribution of multipliers ξ is a triangular one (see text), (*a*) is the result after such a process after 7 iterations, (*b*) is after 10 iterations. Notice that such fields are positive everywhere.

invariance in the inertial range of turbulence becomes a hypothesis of scale-independence of the ξ statistics, and this leads to multifractal behaviour. For a detailed discussion of these issues, see I. Another ingredient implicitly assumed by such cascade models is sweeping: one assumes that an 'eddy' of size r is advecting smaller eddies which originated at earlier times within a large structure upstream during a similar realization of the cascade process.

One can obtain the $f(\alpha)$ curve of such intermittent fields from

$$\alpha(q) = \frac{\langle \xi^q \log_2(\xi) \rangle}{\langle \xi^q \rangle}, \tag{108}$$

$$f[\alpha(q)] = q\alpha(q) + \log_2 \langle \xi^q \rangle + d, \tag{109}$$

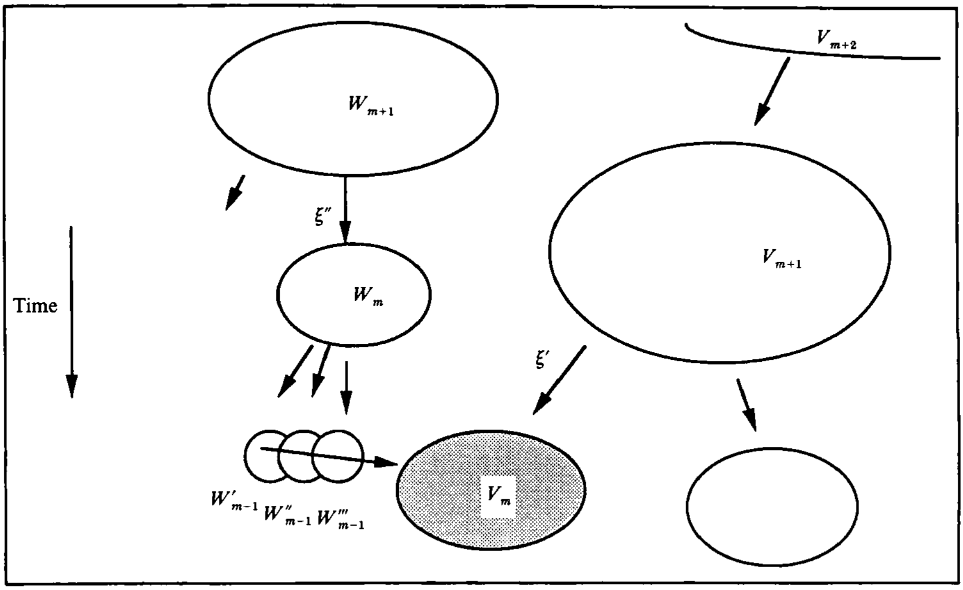

FIGURE 29. Sketch of the mixed cascade model. An eddy V_m is generated by the 'decay' of a larger one (V_{m+1}), receiving a fraction ξ' of the flux of kinetic energy associated with V_{m+1}. At the same time V_m receives a fraction $\gamma < 1$ (a negative contribution) of the flux associated with all the smaller eddies (W'_{m-1}, W''_{m-1} and W'''_{m-1}) that are being convected by V_m.

where the averages are taken over the probability distribution of the random variable ξ. Figure 28 shows 2 stages of $\pi^{(m)}$ implied by such a multiplicative process in one dimension ($d = 1$). A single realization of the process after 7 and 10 steps is shown, and we have used $M = 10$. For the probability density of ξ we used

$$P(\xi) = \begin{cases} 4\xi, & 0 < \xi < \frac{1}{2}; \\ 4(1-\xi), & \frac{1}{2} \leqslant \xi < 1; \\ 0 & \text{otherwise.} \end{cases} \tag{110}$$

This distribution is a good approximation to the measurements of multiplier distributions (Chhabra & Sreenivasan 1990) for one-dimensional sections through fields of dissipation. As remarked earlier, this is a convenient phenomenological model for the intermittency of local rates of dissipation, but it is not expected to be valid for the real flux $\pi^{(m)}$, because the model is never negative.

Now we turn our attention to a physical scenario that can lead to negative flux locally. Let us assume that at some places the flow behaves in a two-dimensional fashion: a collection of small 'eddies', in addition to stretching, wrap around each other in a manner similar to vortex pairing. So in addition to creating smaller scales, the pairing causes some negative flux of kinetic energy to larger scales. There is no *a priori* reason why this could not happen in three-dimensional turbulence. The next question is now to represent such a process in terms of the phenomenological picture of breakdown of 'eddies'.

Consider the situation depicted in figure 29. While an eddy V_m (shaded 'eddy') of size r_m receives some fraction ξ^* of the flux from its bigger predecessor V_{m+1}, it receives a (negative) fraction γ of the flux that was received by all smaller eddies W'_{m-1}, W''_{m-1}, W'''_{m-1} that were created before by eddy W_m and that are presently being swept by eddy V_m. To allow for global conservation, we must impose $\xi^* = (1+\gamma)\,\xi$, where the multiplier ξ is a random variable akin to the multipliers of the traditional forward-only cascade (for which $\langle\xi\rangle = 2^{-d}$). Therefore, we can write the net flux of energy to smaller scales for the eddy V_m as

$$\Pi^{(m)}(V_m) = (1+\gamma)\,\xi'\Pi^{(m+1)}(V_{m+1}) - \gamma\Sigma\Pi^{(m-1)}(W_{m-1}). \tag{111}$$

To compute the flux at scale r_m at some location (as opposed to the situation in (105)) we must take into account the flux at both the large scale and at the smaller convected scales. These convected scales in turn involve the flux at even smaller scales in a similar way, so that the basic physics of such a cascade model involves complicated cross-linking between different cascades occurring at different times, scales and positions. To obtain some quantitative insight into such a process, let us assume that γ is small. Up to first order in γ we express the flux received by eddy V_m in terms of fluxes occurring at scales $r_{(m+1)}$ according to

$$\Pi^{(m)}(V_m) = (1+\gamma)\,\xi'\Pi^{(m+1)}(V_{m+1}) - \gamma\xi''\Pi^{(m+1)}(W_{m+1}). \tag{112}$$

Here ξ' and ξ'' denote different realizations of the random variable ξ and $\Pi^{(m+1)}(W_{m+1})$ is the flux pertaining to an eddy W_{m+1} that existed at some previous time. From (112) it is apparent that without intermittency (if ξ only takes on a single value given by its mean 2^{-d}), $\Pi^{(m)}(V_m)$ could never become negative. However, if ξ is allowed to fluctuate, then even if γ is small $\gamma\xi''\Pi^{(m+1)}(W_{m+1})$ could locally become larger than $(1+\gamma)\,\xi'\Pi^{(m+1)}(V_{m+1})$ and cause negative flux of energy.

Equation (112) defines a recursion which can be closed by assuming that at the largest scale $r = L$, $(m = M)$, the total flux to smaller scales is the (constant) value $\langle\epsilon\rangle L^3$. The net flux through scale r_m for some eddy V_m of size r_m can thus be written as

$$\Pi^{(m)}(V_m) = \langle\epsilon\rangle L^3 \sum_{n=0}^{k} \left\{(1+\gamma)^{k-n}(-\gamma)^n \sum_{l=1}^{\binom{k}{n}} \prod_{j=1}^{k} \xi^{(j,\,l,\,n)}\right\}. \tag{113}$$

Here we have used another scale index k which increases as the scales become smaller:

$$k = M - m. \tag{114}$$

In (113), the $\xi^{(j,\,l,\,n)}$ are independent realizations of ξ for the different indices (j, l, n). We do not neglect higher powers of γ here because they multiply products of ξ's, which can be relatively large.

We can now use the definition of the local exponent α in terms of ξ, α being the singularity strength of a one-way cascade with multipliers ξ:

$$\prod_{j=1}^{k} \xi^{(j)} = \left(\frac{r_m}{L}\right)^{\alpha}. \tag{115}$$

Using this and relation (106), we obtain the flux per unit volume (in d dimensions) at scale r_m and some location X

$$\pi^{(m)}(X) = \langle\epsilon\rangle \sum_{n=0}^{k} \left\{(1+\gamma)^{k-n}(-\gamma)^n \sum_{l=1}^{\binom{k}{n}} \left(\frac{r_m}{L}\right)^{\alpha^{(l,\,n)}-d}\right\}. \tag{116}$$

The sum involves 2^k terms with an independent value of α for each term.

An important condition that must be obeyed by the mixed cascade is that the mean flux averaged over all eddies of a certain scale must be independent of the scale or m and equal to $\langle\epsilon\rangle$. Since $\langle\xi\rangle = 2^{-d}$ it follows from (115) that

$$\left\langle \left(\frac{r_m}{L}\right)^{\alpha-d} \right\rangle = 1, \tag{117}$$

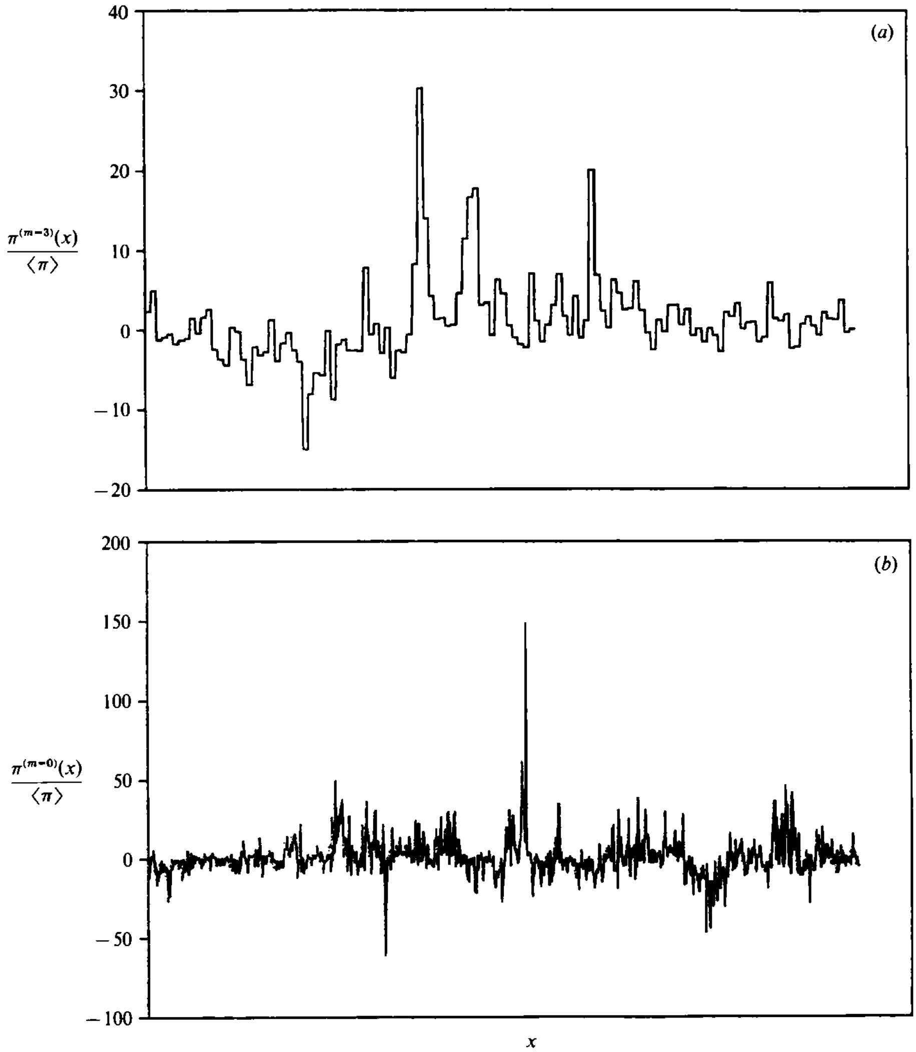

FIGURE 30. Illustration of an intermittent field generated by a multiplicative, but mixed cascade process in one dimension with a triangular distribution of multipliers and with $\gamma = 0.2$ (see text), (*a*) is the result of such a process after 7 iterations, (*b*) is after 10 iterations. Notice that such fields can become negative at many locations, but it still has the property of increasing intermittency at smaller scales.

which implies that

$$\langle \pi^{(m)}(X) \rangle = \langle \epsilon \rangle, \quad \text{for all } m \quad (0 < \gamma < 1). \tag{118}$$

To illustrate some properties of such a process, we generate a one-dimensional version of $\pi^{(m)}(x)$. For this we generate 2^k signals $\pi^{(k)}(x) = (r_m/L)^{\alpha-d}$ in the same fashion as the signal shown in figure 28, each with a different seed for the random multipliers ξ, but selected from the same distribution of (110). These signals are then added point by point according to (116). The result is shown in figure 30 for $m = 3$ and $m = 0$ (corresponding to $k = 7$ and $k = 10$) for $\gamma = 0.2$. The intermittency increases with decreasing scale r_m, but the flux is negative at many locations.

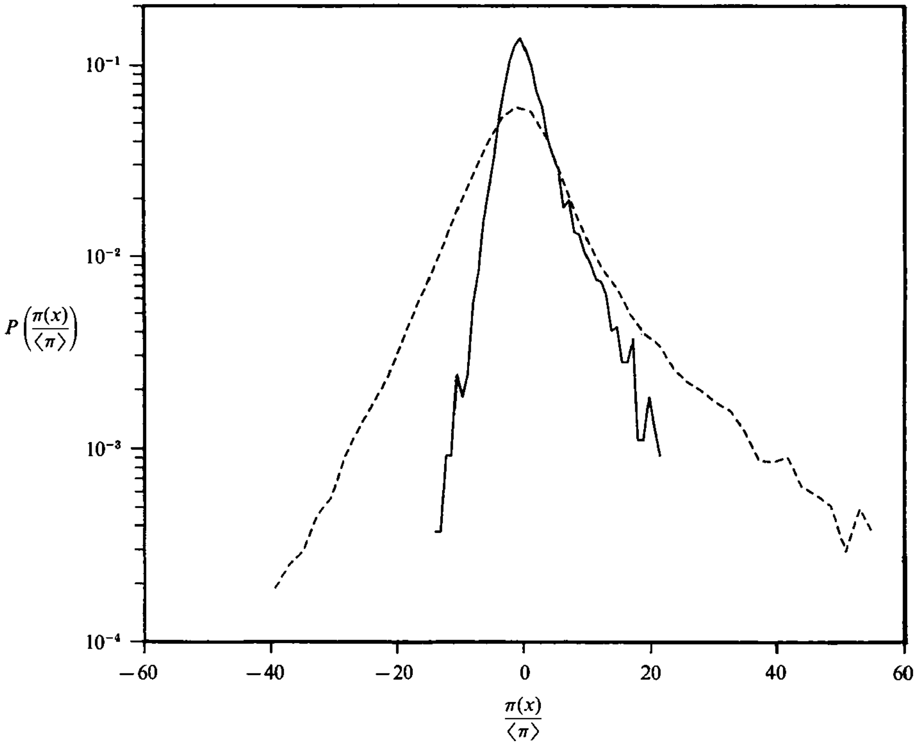

FIGURE 31. Probability density distribution for the flux π obtained from the two realizations of the mixed cascade model. ——, 7 steps (scale $m = 3$ or $r_m = 8$); ---, 10 steps (scale $m = 10$ or $r_m = 1$). Notice that the tails become increasingly longer as the scales become smaller.

Next we obtain the probability density of $\pi^{(m)}(x)$ at the two levels shown in the previous figures. The result is shown in figure 31. The exponential tails and the Gaussian central region are quite consistent with the behaviour of the real local flux computed in §5.2. The fraction of space where $\pi^{(m)}(x) < 0$ is always very close to 0.5, independent of the value of γ at large k. One difference is a slight asymmetry in the probability density functions, the right-hand tail being somewhat longer than the one on the negative side. The distributions become more symmetric with increasing values of γ (and by construction the negative side vanishes for $\gamma \rightarrow 0$).

Notice that in the model the total flux is the same at every scale, as opposed to the three-dimensional simulations. This is due to the low Reynolds numbers which precludes the existence of an inertial subrange (in which the nonlinear flux would be expected to be a constant equal to the rate of dissipation). For this reason we do not attempt a comparison between observations and the parameters of the mixed cascade model. However, we find it interesting that it is possible to generate fields which become more intermittent in a multiplicative fashion, and exhibit negative values at many places.

We point out that the recent backscatter model of Leith (1990) exhibits Gaussian white-noise statistics. In the present model, non-Gaussian structure and two-point correlations arise by the multiplicative process involved (the flux at nearby points is correlated because small nearby eddies may share a common 'ancestor', see Meneveau & Chhabra 1990). Nevertheless, it is at present not clear how one could use this ingredient to formulate improved subgrid-scale models, since we do not know how to correlate the subgrid structure with the large scales.

Finally, we remark that the primary ingredient of the present mixed cascade model is mathematical rather than physical: it is the additive mixing of multifractals which produces a more Gaussian-type behaviour near the mean, while maintaining the non-Gaussian tails. The physical picture leaves much room for improvement. For instance, one problem with the present model is that small eddies are generated regardless of the sign of the flux. It would also be of interest to examine the issue of backscatter in the context of intermittency models such as the one recently proposed by She (1991).

8. Summary and conclusions

We have explored the usefulness of the wavelet transform in analysing turbulent flow fields. Because of the simultaneous resolution of scale and position, several issues related to intermittency and spatial distribution could be addressed. The wavelet transformed Navier–Stokes equations were shown to be rather complicated but the appropriate contraction relevant to the energetics of turbulence was more transparent. We stressed the need to use discrete orthonormal wavelets for practical applications, as well as the importance of statistical analysis of the resulting spatial distributions.

In this spirit we introduced the dual spectra, which measure the contribution of each scale and its spatial variability. These can be used to quantify the intermittency of the kinetic energy for example. It was shown that the local kinetic energy could be described as a multifractal field. The measured $f(\alpha)$ curve of the kinetic energy was consistent with the results of dimensional analysis applied to the dissipation field, but only for the high-intensity part of the distribution. Since the energy could locally be zero, the behaviour at small values was fundamentally different to that of the dissipation.

We then defined local transfer and flux of kinetic energy in the orthonormal wavelet representation and computed them in direct numerical simulations of turbulence. Strong spatial fluctuations were observed, their mean spectral value being quite unrepresentative of local values. It was shown that while $\pi(r, \boldsymbol{x})$, the flux of kinetic energy through a scale r at location $\boldsymbol{x}$, is positive on the average, large deviations from its average value were observed, with typical standard deviations of the order of 4 to 5 times the mean. These features were shown to be robust with respect to the precise wavelet used. One wavelet tested was essentially a sharp Fourier band-pass filter in octaves (Fourierlet), suggesting that statistical results obtained by such approaches (e.g. the study of Domaradski & Rogallo 1990) give results that are comparable to the ones using wavelet analysis.

By appropriately decomposing the nonlinear terms of the Navier–Stokes equation, we could subtract the transfer (and flux) due to the interactions among large scales from the total values. This allowed the definition of a dual bispectrum of transfer and the definition of a local effective eddy viscosity and of the 'subgrid' flux of energy $\pi_{sg}(r, \boldsymbol{x})$, involving scales smaller than r, at location $\boldsymbol{x}$. All of these quantities exhibited intermittent spatial behaviour, with exponential tails in their probability distributions, while their spatial mean values were consistent with the usual spectral behaviour. The importance of exponential tails in turbulence (Narashima 1989) is confirmed by these observations. Quite significantly, large negative values of $\pi_{sg}(r, \boldsymbol{x})$ were observed, implying local inverse energy flux from small to large scales of motion. Although these results have been obtained for low-Reynolds number flows where no fully developed inertial range exists, it seems unlikely that the local backscatter would disappear at higher Reynolds number. In fact, the analysis of channel flow by Piomelli *et al.* (1991) suggests a modest increase of backscatter with Reynolds number. The general picture of turbulence that is confirmed by the present analysis is that there is strong spatial intermittency in nonlinear quantities; their mean spectral behaviour resulting from a delicate balance between large positive and negative excursions. The wavelet analysis is a way of quantifying these observations in a standardized fashion by using 'flow-independent eddies' to decompose the velocity field.

We have proposed a simple extension to the traditional cascade models of energy, which allows for backscatter (negative energy flux) in an intermittent fashion. The model suggests (but does not prove) that the detailed spatial statistics of the backscatter are intimately linked to the intermittency of the cascade. In the mixed cascade model, if there was no intermittency (as in the original Kolmogorov (1941) picture), there would also not be negative flux. Only the strong spatial fluctuations produced by intermittency allow some small scales to be very 'active', so that if they pair (passing a part of their flux of energy to the larger scale) the resulting negative flux may locally overwhelm the positive one. We have shown that such mixed cascade models exhibit the same qualitative features as the real local flux: increasing intermittency at decreasing scale, exponential-like tails of the probability density for both positive and negative values. However, measurements of $\pi^{(m)}(x)$ need to be made at higher Reynolds numbers before we can make more quantitative comparisons with such mixed cascade models.

In summary, the present study shows that orthonormal wavelet analysis can be performed just as easily as Fourier analysis, and we believe the physical interpretation of the wavelet coefficients is more natural to the phenomenon of turbulence than the coefficients of globally extended functions such as Fourier modes. As remarked by Stewart (1989), one is decomposing the motion into 'solitons', a concept more appropriate than waves for nonlinear phenomena.

This work was performed while the author was at the Center for Turbulence Research (Stanford University & NASA Ames Research Center), where many thanks are due to Professor P. Moin for his numerous suggestions, and for many stimulating conversations on this topic. I am indebted to Dr M. Rogers for his help and for making available his simulations of homogeneous shear flow, as well as to Dr R. Rogallo for providing me with his simulation of decaying isotropic turbulence, for very interesting discussions and for his very detailed reading of a prior version of this manuscript. I have greatly benefited from comments and conversations with Professors A. Grossmann, W. C. Reynolds, J. Ferziger, U. Frisch, Drs M. Farge, J. van der Vegt, S. Veeravalli, and Mr M. Krishnan. The financial support from the Center for Turbulence Research is greatly appreciated.

Note added in proof. Recently, Yamada & Ohkitani (1990) have also used orthonormal wavelets to analyse energy spectra in measurements of atmospheric turbulence.

REFERENCES

Arneodo, A., Grasseau, G. & Holschneider, M. 1988 *Phys. Rev. Lett.* **61**, 2287.

Barcy, E., Arneodo, A., Frisch, U., Gagne, Y. & Hopfinger, E. 1990 In *Turbulence and Coherent Structures* (ed. O. Metais & M. Lesieur), p. 203. Kluwer.

Batchelor, G. K. & Townsend, A. A. 1949 *Proc. R. Soc. Lond.* A **199**, 238.

Benzi, R., Paladin, G., Parisi, G. & Vulpiani, A. 1984 *J. Phys.* A **17**, 3521.

CHHABRA, A. & SREENIVASAN, K. R. 1991 *Phys. Rev.* A **43**, 1114.

DAUBECHIES, I. 1988 *Commun. Pure Appl. Math.* **41**, 909.

DOMARADSKI, J. A. & ROGALLO, R. 1990 *Phys. Fluids* A**2**, 413.

EVERSON, R., SIROVICH, L. & SREENIVASAN, K. R. 1990 *Phys. Lett.* A**145**, 314.

FARGE, M. 1992 *Ann. Rev. Fluid Mech.* (to appear).

FARGE, M. & RABREAU, G. 1988 *C. R. Acad. Sci. Paris* 2, **307**, 1479.

FRISCH, U., SULEM, P. L. & NELKIN, M. 1978 *J. Fluid Mech.* **87**, 719.

GAGNE, Y. 1989 PhD thesis, University of Grenoble.

GROSSMANN, A. & MORLET, J. 1984 *SIAM J. Math. Anal.* **15**, 723.

KENNEDY, D. A. & CORRSIN, S. 1961 *J. Fluid Mech.* **10**, 366.

KOLMOGOROV, A. N. 1941 *C. R. Acad. Sci. USSR* **30**, 301.

KOLMOGOROV, A. N. 1962 *J. Fluid Mech.* **62**, 82.

KRAICHNAN, H. 1974 *J. Fluid Mech.* **62**, 305.

KRAICHNAN, H. 1976 *J. Atmos. Sci.* **33**, 1521.

KRONLAND-MARTINET, R., MORLET, J. & GROSSMANN, A. 1987 *Intl J. Patt. Rec. Art. Intel.* **1**, 97.

LEITH, C. E. 1990 *Phys. Fluids* A**2**, 297.

LEONARD, A. 1974 *Adv. Geophys.* **18A**, 237.

LESLIE, D. C. & QUARINI, G. L. 1979 *J. Fluid Mech.* **91**, 65.

LUMLEY, J. 1967 In *Atmospheric Turbulence and Radio Wave Propagation* (ed. A. M. Yaglom & J. L. Tatarsky), p. 1668. Moscow.

MALLAT, S. J. 1989 *IEEE Patt. Anal. Mach. Int.* **11**, 674.

MANDELBROT, B. B. 1974 *J. Fluid Mech.* **62**, 331.

MENEVEAU, C. 1990 CTR manuscript 120 (available from the author).

MENEVEAU, C. 1991 *Phys. Rev. Lett.* **66**, 1450.

MENEVEAU, C. & CHHABRA, A. 1990 *Physica* A**164**, 564.

MENEVEAU, C. & SREENIVASAN, K. R. 1987*a* *Nucl. Phys.* B *Proc. Suppl.* **2**, 49.

MENEVEAU, C. & SREENIVASAN, K. R. 1987*b* *Phys. Rev. Lett.* **59**, 1424.

MENEVEAU, C. & SREENIVASAN, K. R. 1991 *J. Fluid Mech.* **224**, 429.

MEYER, Y. 1986 In *Seminaire Bourbaki*, p. 662.

MIN DUONG-VAN 1987 *Nucl. Phys.* B *Proc. Suppl.* **2**, 521.

NAKANO, T. 1988 *Phys. Fluids* **31**, 1420.

NARASHIMA, R. 1989 In *Whither Turbulence, or Turbulence at Crossroads* (ed. J. L. Lumley). Springer.

NELKIN, M. 1989 *J. Stat. Phys.* **54**, 1.

NOVIKOV, E. A. 1971 *Appl. Math. Mech.* **35**, 231.

ORSZAG, S. A. & PATTERSON, G. S. 1972 *Phys. Rev. Lett.* **28**, 76.

PARISI, G. & FRISCH, U. 1985 In *Turbulence and Predictability in Geophysical Fluid Dynamics and Climate Dynamics*, p. 84. North-Holland.

PIOMELLI, U., CABOT, W. H., MOIN, P. & LEE, S. 1991 *Phys. Fluids* A **3**, 1766.

ROGALLO, R. 1982 *NASA Tech. Memo.* 81315.

ROGALLO, R. & MOIN, P. 1984 *Ann. Rev. Fluid Mech.* **16**, 99.

ROGERS, M. & MOIN, P. 1986 *J. Fluid Mech.* **176**, 33.

ROGERS, M., MOIN, P. & REYNOLDS, W. C. 1976 *TF25*. Dept. of Mech. Engng, Stanford University, CA 94305.

ROSE, H. 1977 *J. Fluid Mech.* **81**, 719.

SIGGIA, E. D. 1977 *Phys. Rev.* A**15**, 1730.

SHE, Z. S. 1991 *Phys. Rev. Lett.* **66**, 600.

STEWART, I. 1989 *Nature* **338**, 18.

SULEM, P. & FRISCH, U. 1975 *J. Fluid Mech.* **72**, 417.

YAMADA, M. & OHKITANI, K. 1990 *Prog. Theor. Phys.* **83**, 819.

ZIMIN, V. D. 1981 *Izv. Atmos. Oceanic Phys.* **17**, 941.